C0-IPM with generalised periodicity and application to flexoelectricity-based 2D metamaterials

Oscar Balcells-Quintana · David Codony · Sonia Fernández-Méndez

Abstract We propose a methodology to solve high-order PDE boundary value problems with generalised periodicity, in the framework of the $\mathcal{C}^0$ interior penalty method. The method is developed for the analysis of flexoelectricity-based metamaterial unit cells, formalising the corresponding problem statement and weak form, and giving details on the implementation of the local and macro conditions for generalised periodicity. Numerical examples demonstrate the high-order convergence of the method and its applicability in realistic problem settings.

Keywords generalised periodicity · unit cell · metamaterial · 4th order PDE · $\mathcal{C}^0$ finite elements · interior penalty method · strain gradient elasticity · flexoelectricity

1 Introduction

Metamaterials are defined, in a broad sense, as materials that are engineered to exhibit properties which are not found in naturally occurring materials [14]. They can be built by assembling multiple base materials (plastics, metals, etc) and voids, in repeated spatial patterns at small scales. Thus, the interesting features of metamaterials are not driven by the properties of the base materials they are made of, but from its particular artificial structure. The raising interest in the design of metamaterials has boosted research efforts

O. Balcells-Quintana and S. Fernández-Méndez
Laboratori de Càlcul Numèric, E.T.S. de Ingeniería de Caminos, Universitat Politècnica de Catalunya (UPC), Barcelona, Spain
E-mail: oscar.balcells@estudiant.upc.edu, sonia.fernandez@upc.edu

D. Codony
Centre Internacional de Mètodes Numèrics en Enginyeria (CIMNE), Barcelona, Spain
E-mail: dcodony@cimne.upc.edu

from a theoretical standpoint [23], and also in the development of mathematical and computational models capable of capturing small scale phenomena. In particular, the geometrical design of flexoelectrictity-based metamaterials, to accumulate flexoelectric effects from small scale to macro scale, has recently become an active field of research. The goal is to achieve an apparent piezoelectric macroscopic response in metamaterials made of non-piezoelectric constituents [13,18,17,7,3,15].

Flexoelectricity is a two-way electromechanical coupling, present in all dielectrics, that is relevant only at small scales [20], and can be modelled by a set of fourth-order Partial Differential Equations (PDEs) with proper boundary conditions. There are several approaches in the literature for the solution of fourth-order PDEs and, in particular, for the solution of flexoelectricity problems, such as mixed finite element methods [16,10], meshless methods [1], $\mathcal{C}^1$ approximations on regular grids with embedded domains [13,18,8,22,17,9] or $\mathcal{C}^0$ interior penalty finite element methods (C0-IPM) [21].

In [21] the authors derive a new formulation for the solution of the flexoelectricity problems in finite domains, based on the C0-IPM method initially proposed for biharmonic equations [4,5,11]. Its good performance is experimentally tested with synthetic problems and with realistic beam problems. The C0-IPM method considers a standard $\mathcal{C}^0$ finite element (FE) approximation space, with degree $p \geq 2$. Continuity of the normal derivatives and equilibrium of forces, between elements and on the mesh vertexes, are imposed in weak form, by means of the introduction of integrals on the element sides (faces in 3D). The main potential advantages of C0-IPM in front of other methods are that *(i)* no additional unknowns are introduced, and *(ii)* meshes can fit to the boundary avoiding the ill-conditioning issues, and the costly numerical integration, typical in embedded methods with cropped elements. Moreover, as a FE method, numerical integration is straight-forward, prescribed values of the solution can be directly enforced setting nodal values, material interfaces do not need any special treatment as long as the mesh fits to the interface, and meshes can be refined where needed to capture features in the solution. In particular, in the presence of boundary layers in the electric field, an anisotropic FE mesh can be considered to refine along the boundary only in the orthogonal direction, as shown in the flexoelectric beam simulations in [21]. As expected for a C0-IPM formulation for a fourth-order PDE problem [4,5,12], the convergence rates are close to the convergence rates of standard FEM in second-order PDEs. More precisely, the convergence tests in [21] exhibit rates between p and $p+1$ when a p-th degree FE approximation is used, for $p = 3, 4$.

Given the good performance and flexibility of the method proposed in [21], the goal of this work is to provide an efficient alternative for the computational design of flexoelectricity-based metamaterials, by reducing the C0-IPM formulation in infinite metamaterial domains to a single unit cell. This leads to the formalization and incorporation of the Generalised Periodicity (GP) conditions into the standard C0-IPM formulation in [21].

For the sake of conciseness, all derivations are done for 2D flexoelectricity, and initially assuming GP in both directions. The methodology can, however, be directly applied in 3D with further implementation effort, and to strain-gradient elasticity problems, just setting to zero the flexoelectricity and piezoelectricity coefficients. The reduction to GP in only one direction is straightforward and it is commented later.

The GP concept for the computational modelling of metamaterials built by repetition of a unit cell, is formalised in section 2, together with the conditions for a proper computational unit cell. The problem statement in the unit cell is then presented in section 3, with the introduction of the GP conditions on the boundary of the rectangle, so that the problem statement in the unit cell is equivalent to the problem in the infinite metamaterial domain. The intersection of the infinite domain with the boundary of the unit cell rectangle is treated as an artificial interface, and high-order interface conditions are stated relating the left and right boundaries, the bottom and top boundaries, and the corners on the rectangle boundary.

Section 4 focuses on the derivation of the weak form with GP conditions. First, the functional space complying with the GP jump conditions (for the components of the displacement and for the electric potential) is defined as the set of functions with constant difference between the left and right boundaries, and between the bottom and top boundaries. Some properties of the GP space, useful for the derivation of the weak form, are also stated. The weak form is then derived using the rationale that standard C0-IPM applies on interior faces and vertexes, translated now to the artificial boundaries and vertexes. That is, continuity of the normal derivative of the displacement, equilibrium of forces and conservation of electric charge are imposed in weak form, across artificial boundaries in the unit cell, and also on the corners of the rectangle if they are not in a material void. Using the properties of the GP space and the GP conditions, it is proved that the new terms arising on the artificial boundaries cancel out or can be simplified. Very conveniently, the resulting weak form with GP conditions has an expression very close to the standard C0-IPM one, just adding the Dirichlet macro-conditions, and extending the integrals on the interface between elements to include also integrals on the bottom and left boundaries, with a proper extension of the definition of the jump and mean operators. As a side result of the weak form derivation, Neumann macro-conditions are identified, as quantities dual to the jump of the displacement or the potential, in each direction of the unit cell.

Computational aspects are commented in section 5, detailing the steps to pleasantly adapt an existing C0-IPM code to incorporate GP conditions. The considered strategy assumes that the computational mesh is such that the nodes and sides on the artificial boundaries fulfill the periodicity of the unit cell geometry. Thus, as naturally done for the solution of second order PDEs, the difference of the nodal values on the top and bottom boundaries (or on the left and bottom boundaries) is set to a constant, that can be prescribed or left as an unknown of the problem, reducing the approximation space and the consequent system of equations. However, flexoelectricity modeling involves fourth-order

PDEs, thus integrals on the artificial GP boundary have to be incorporated in the system to account for the high-order continuity and equilibrium conditions. These integrals can be accounted for in the code in a straight-forward manner, just adding the artificial GP faces in the list of interior faces.

This work does not cover the case of FE meshes with non-matching sides at the top and bottom boundaries, and at the left and right boundaries. In the case of non-matching sides, the continuity and equilibrium conditions could be imposed in weak form, as in [3], with non-negligible implementation effort. On other hand, the strategy considered here for the calculation of apparent macroscopic properties is the one adopted in [17]. Alternative strategies based on homogenization, as the ones compared in [19], could also be considered. The chosen one is, however, naturally integrated in the C0-IPM formulation and implementation, and it is suitable for any kind of geometry, also with unstructured meshes.

Numerical tests demonstrate the applicability and good performance of the proposed formulation with GP conditions. First, a convergence test with synthetic solution shows how the proposed formulation for problems with GP maintains the high-order convergence and accuracy of the C0-IPM method. Second, two numerical examples show that the numerical solutions with the proposed methodology are in agreement with the physics: the solution in a unit cell with GP properly captures the solution of an infinite metamaterial, as the limit for increasing number of concatenated cells, and it is independent of the selected unit cell. Finally, some of the numerical experiments in [17] are reproduced, showing qualitative agreement in the results.

2 Generalised Periodicity and unit cell

Metamaterials can be built by reproducing a certain pattern in space, or equivalently, by infinitely concatenating a unit cell, as illustrated in the sketch in Figure 1.

When considering an electroactive metamaterial with periodic geometric structure in all directions, one expects the same periodic repetition, *up to constants*, in the displacement and the electric potential, which leads to periodic strain and electric fields. This idea is formalised in this section by introducing the concepts of generalised periodicity and unit cells, and some properties derived from their definitions.

2.1 Generalised periodicity

Definition 1 (GP function) We say that a function $f : \mathbb{R}^n \to \mathbb{R}$ has *generalised periodicity* (GP), or that it is a *GP function*, of *multi-period* $\boldsymbol{L} = (L_1, ..., L_n)$, with *multi-increment* $\boldsymbol{\Delta} = (\Delta_1, ..., \Delta_n)$, if

$$f(\boldsymbol{x} + L_i \mathbf{e}_i) = f(\boldsymbol{x}) + \Delta_i, \qquad \text{for } 1 \leq i \leq n, \quad \forall \boldsymbol{x} \in \mathbb{R}^n,$$

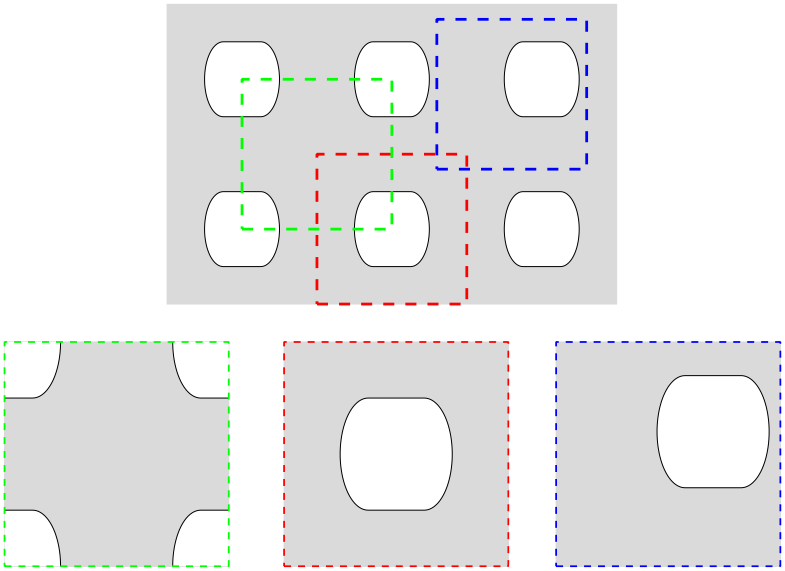

Fig. 1 Example of a 2D domain with periodic geometry, and three different possible choices of a unit cell representative. All of them give the same 2D pattern when infinitely concatenated.

where $\mathbf{e}_i$ is the i-th canonical vector of $\mathbb{R}^n$, and the *jumps* Δ_i are the components of the multi-increment. It can also be written as

$$f(\boldsymbol{x} + L_i \mathbf{e}_i) = f(\boldsymbol{x}) + L_i \delta_i, \qquad \text{for } 1 \leq i \leq n, \quad \forall \boldsymbol{x} \in \mathbb{R}^n,$$

with the jumps per unit length defined as $\delta_i = \Delta_i / L_i$.

As a direct consequence of the definition, by simply applying it repeatedly in several directions, we have

$$f(\boldsymbol{x} + \sum_{i=1}^{n} k_i L_i \mathbf{e}_i) = f(\boldsymbol{x}) + \sum_{i=1}^{n} k_i \Delta_i, \qquad \forall \boldsymbol{x} \in \mathbb{R}^n, \; k_i \in \mathbb{K}.$$

Thus, a GP function is completely determined in $\mathbb{R}^n$ from its value at a *unit cell*, that is, in any rectangle (rectangular cuboid in 3D) with side (edge) lenghts $\{L_i\}_{i=1}^n$, as illustrated in figure 2 (left). In other words, the solution on a metamaterial with periodic geometry with multi-period $\boldsymbol{L}$, can be obtained solving just on a unit cell, as illustrated in figure 2 (right), with proper GP boundary conditions.

Finally, the following result provides an alternative characterization of GP functions, that will be considered for the definition of synthetic analytical solutions for numerical convergence tests.

Lemma 1 *A function f is GP of multi-period $\boldsymbol{L} \in \mathbb{R}^n$ iff there exist $\boldsymbol{\delta} \in \mathbb{R}^n$ and a periodic function f^p with multi-period $\boldsymbol{L}$ such that*

$$f(\boldsymbol{x}) = f^p(\boldsymbol{x}) + \boldsymbol{\delta} \cdot \boldsymbol{x}.$$

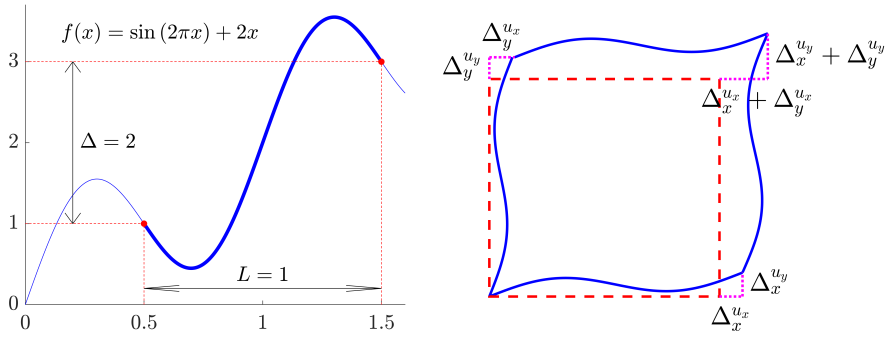

Fig. 2 Example of a 1D GP function with period $L = 1$ and jump $\Delta = 2$ (left), and deformation of a square unit cell with multi-period $L = (1, 1)$ (right), detailing the displacement at each corner in terms of the jumps. The deformation is the same at the top and bottom boundaries, and at the left and right boundaries.

Proof The implication to the left is trivial. Assume $f(\boldsymbol{x}) = f^p(\boldsymbol{x}) + \boldsymbol{\delta} \cdot \boldsymbol{x}$ with f^p periodic of multi-period $\boldsymbol{L} \in \mathbb{R}^n$, and $\boldsymbol{\delta} \in \mathbb{R}^n$. Then f is indeed GP, since

$$f(\boldsymbol{x} + L_i \mathbf{e}_i) = f^p(\boldsymbol{x} + L_i \mathbf{e}_i) + \boldsymbol{\delta} \cdot (\boldsymbol{x} + L_i \mathbf{e}_i) = f(\boldsymbol{x}) + L_i \delta_i.$$

For the implication to the right, assume f is GP and take the candidate $f^p(\boldsymbol{x}) := f(\boldsymbol{x}) - \boldsymbol{\delta} \cdot \boldsymbol{x}$. Then f^p is indeed periodic of multi-period $\boldsymbol{L} \in \mathbb{R}^n$, since

$$f^p(\boldsymbol{x}+L_i\mathbf{e}_i) = f(\boldsymbol{x}+L_i\mathbf{e}_i) - \boldsymbol{\delta}\cdot(\boldsymbol{x}+L_i\mathbf{e}_i) = f(\boldsymbol{x}) + L_i\delta_i - \boldsymbol{\delta}\cdot(\boldsymbol{x}+L_i\mathbf{e}_i) = f^p(\boldsymbol{x}). \square$$

2.2 2D unit cells

For the sake of simplicity, from now on, we restrict all the derivations and analysis to the two-dimensional metamaterials scenario. The proposed methodology can be directly applied also to 3D, without further theoretical developments, but requiring additional implementation effort. With this mindset, if not otherwise stated, the domain Ω is a perforated solid 2D rectangle, that is, $\Omega \subset (0, L_x) \times (0, L_y) \subset \mathbb{R}^2$, corresponding to a unit cell.

It will come in handy to have an adequate nomenclature for the parts of the boundary of the unit cell and, since an image is worth a thousand words, we refer to Figure 3 (right), which compels this nomenclature in a typical example of a unit cell geometry.

More precisely, $\mathcal{S}$, $\mathcal{N}$, $\mathcal{W}$ and $\mathcal{E}$, are the bottom, top, left and right sides of the domain Ω. They are artificial boundaries, in the sense that they would not be boundaries in the infinite domain. Differently, the inner boundary $\partial\Omega^i$, in pink, is a physical boundary also present in the infinite domain. We also denote by $\mathcal{C}^R := \{C_k^R\}_{k=1}^{n_R}$, $\mathcal{C}^F := \{C_k^F\}_{k=1}^{n_F}$, and $\mathcal{C}^T := \{C_k^T\}_{k=1}^{n_T}$, the sets of rectangle, false, and true corners, respectively. By geometry periodicity in both directions, the number of physical rectangle corners is $n_R = 0$ if the corners

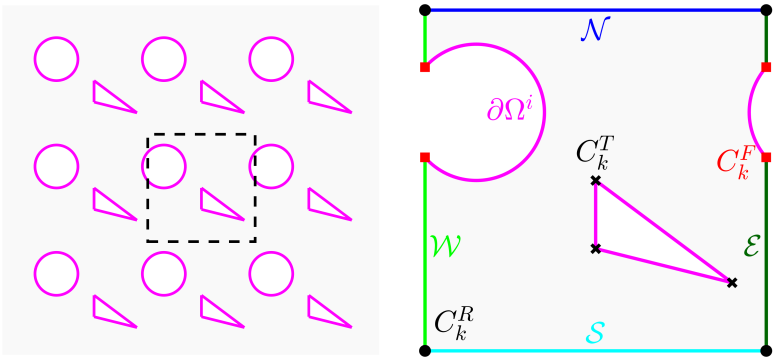

Fig. 3 Example of infinite domain (left) defined by the repetition of the unit cell on the right, and representation of the boundary and corners nomenclature in the unit cell (right).

of the rectangle are in a material void, and $n_R = 4$ otherwise. True corners, $\mathcal{C}^T$, are physical corners that would also be present in the infinite domain; whereas false corners, $\mathcal{C}^F$, are artificial corners that only appear when a unit cell representative is sliced. We also assume $\partial\Omega^i$ to be a finite union of smooth curves, not including its singular points if any, i.e, it does not include the corners $\mathcal{C}^R \cup \mathcal{C}^F \cup \mathcal{C}^T$.

Obviously, there are some conditions for a computational domain Ω to be a proper unit cell, corresponding to a periodic geometry when concatenated. We will say that Ω is a *valid unit cell* if its sides satisfy the *geometry periodicity condition*

$$\mathcal{E} = \{(L_x, y) : (0, y) \in \mathcal{W}\}, \qquad \text{and} \qquad \mathcal{N} = \{(x, L_y) : (x, 0) \in \mathcal{S}\}. \quad (1)$$

Remark 1 Thanks to the geometry periodicity condition, the false corners $\mathcal{C}^F$ always appear in pairs which are in opposed sides of the unit cell, and either vertically or horizontally aligned. That is, for every false corner $C_i^F \in \mathcal{C}^F$, there exists a unique false corner $C_j^F \in \mathcal{C}^F \setminus C_i^F$ such that $C_i^F - C_j^F \in \{(\pm L_x, 0), (0, \pm L_y)\}$.

An additional constraint on the unit cell is added to reduce the cases and simplify the derivations in the problem statement in section 3, and in the corresponding weak form in section 4. We will assume that physical (true) corners are not on the boundary of the rectangle $(0, L_x) \times (0, L_y)$, and that there are no tangencies of the physical boundary with the boundary of the rectangle. In this situation, the boundary of the computational domain Ω is the *disjoint* union

$$\partial\Omega = \mathcal{S} \sqcup \mathcal{N} \sqcup \mathcal{W} \sqcup \mathcal{E} \sqcup \partial\Omega^i \sqcup \mathcal{C}^R \sqcup \mathcal{C}^F \sqcup \mathcal{C}^T.$$

Consequently, false corners sew the physical boundary on consecutive cells with $\mathcal{C}^1$ continuity, i.e with continuous normal and tangent vectors, because they do not coincide with physical true corners.

Figure 4 depicts two non-valid unit cells. The case shown on the left violates the translation condition (1) on the $\mathcal{W}$ and $\mathcal{E}$ sides. In both cases, the additional condition of non-having a physical true corner on the boundary of the rectangle is not satisfied. These two non-valid choices of unit cell representative generate the same spatial pattern represented in Figure 3 (left), when infinitely concatenated in the $\mathbb{R}^2$ plane, for which a valid unit cell can easily be selected, making sure that no physical true corner is on the boundary of the rectangle, as shown in Figure 3 (right). We highlight this fact to loosely claim that one can always choose a valid unit cell representative, at least for patterns that are realistic in an engineering sense.

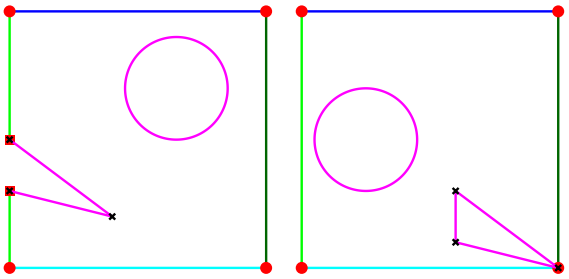

Fig. 4 Examples of non-valid unit cells. Physical true corners (x) should not be on the boundary of the rectangle.

3 Flexoelectricity problem statement with GP conditions

This section focuses on the statement of the flexoelectricity problem with GP conditions. We consider the flexoelectricity model in [21], but the GP conditions stated next can also be applied to other flexoelectricity models. For the sake of conciseness, in this section and next derivations, GP is assumed in both directions, since reducing to the case of GP in one direction is straightforward, as commented in section 4.5.

The problem statement with GP consists on finding the displacement, $\boldsymbol{u} = (u_x, u_y)^T$, and the electric potential, ϕ, satisfiying the partial differential equations (PDEs)

$$\boldsymbol{\nabla} \cdot (\hat{\boldsymbol{\sigma}}(\boldsymbol{u}, \phi) - \boldsymbol{\nabla} \cdot \tilde{\boldsymbol{\sigma}}(\boldsymbol{u}, \phi)) + \boldsymbol{b} = \boldsymbol{0} \quad \text{in } \Omega, \tag{2a}$$

$$\boldsymbol{\nabla} \cdot \hat{\boldsymbol{D}}(\boldsymbol{u}, \phi) - q = 0 \quad \text{in } \Omega, \tag{2b}$$

subject to the *physical boundary conditions*

$$\left.\begin{array}{l} \boldsymbol{t}(\boldsymbol{u}, \phi) = \boldsymbol{0} \\ \boldsymbol{r}(\boldsymbol{u}, \phi) = \boldsymbol{0} \\ w(\boldsymbol{u}, \phi) = 0 \end{array}\right\} \quad \text{on } \partial\Omega^i, \tag{3a}$$

$$\boldsymbol{j}(\boldsymbol{u}, \phi) = \boldsymbol{0} \quad \text{on } \mathcal{C}^T, \tag{3b}$$

the *GP jump constraints*

$$\left.\begin{aligned}\boldsymbol{u}(L_x,y)&=\boldsymbol{u}(0,y)+\boldsymbol{\Delta}_x^{\boldsymbol{u}}\\ \phi(L_x,y)&=\phi(0,y)+\Delta_x^{\phi}\end{aligned}\right\}\ \text{for } (0,y) \text{ on } \mathcal{W},$$
$$\left.\begin{aligned}\boldsymbol{u}(x,L_y)&=\boldsymbol{u}(x,0)+\boldsymbol{\Delta}_y^{\boldsymbol{u}}\\ \phi(x,L_y)&=\phi(x,0)+\Delta_y^{\phi}\end{aligned}\right\}\ \text{for } (x,0) \text{ on } \mathcal{S}, \tag{4}$$

the *GP interface conditions* on the sides

$$\left.\begin{aligned}[\![\partial\boldsymbol{u}/\partial\boldsymbol{n}]\!]&=\boldsymbol{0}\\ [\![\boldsymbol{t}(\boldsymbol{u},\phi)]\!]&=\boldsymbol{0}\\ [\![\boldsymbol{r}(\boldsymbol{u},\phi)\otimes\boldsymbol{n}]\!]&=\boldsymbol{0}\\ [\![w(\boldsymbol{u},\phi)]\!]&=\boldsymbol{0}\end{aligned}\right\}\ \text{on } \mathcal{W}\cup\mathcal{S}, \tag{5}$$

the *GP interface conditions* on the rectangle corners $\mathcal{C}^R$ (provided that $\mathcal{C}^R\neq\emptyset$) and on the false corners $\mathcal{C}^F$ (provided that $\mathcal{C}^F\neq\emptyset$)

$$\{\boldsymbol{j}(\boldsymbol{u},\phi)\}=\boldsymbol{0}\quad\text{on } (\mathcal{C}^F\cup\mathcal{C}^R)\cap\left(\overline{\mathcal{W}}\cup\overline{\mathcal{S}}\right), \tag{6}$$

and the *macro-conditions* commented in remark 2, all together with the definitions of the operators, vectors and tensors explained next.

The mean, $\{\cdot\}$, and jump, $[\![\cdot]\!]$, operators appearing in these equations are defined on the left and bottom sides as

$$\left.\begin{aligned}\{f\}(0,s)&:=(f(L_x,s)+f(0,s))/2\\ [\![f]\!](0,s)&:=f(L_x,s)+f(0,s)\end{aligned}\right\}\quad\text{if } (0,s)\in\overline{\mathcal{W}}$$
$$\left.\begin{aligned}\{f\}(s,0)&:=(f(s,L_y)+f(s,0))/2\\ [\![f]\!](s,0)&:=f(s,L_y)+f(s,0)\end{aligned}\right\}\quad\text{if } (s,0)\in\overline{\mathcal{S}} \tag{7}$$

the jump always involving an odd appearance of the normal vector, so that there is always a change of sign, i.e. a jump operation.

The PDEs (2) and the physical boundary conditions (3) are the usual ones in standard flexoelectricity boundary value problems [21]. Homogeneous natural boundary conditions are assumed on the whole physical boundary, since this is the usual case in metamaterial computations. The treatment of other physical boundary conditions is not considered for the sake of simplicity, but they can also be incorporated as in the standard problem, as commented in section 4.5. In these equations, using Einstein's notation (repeated indexes sum over spatial dimensions), the local and double stress tensors, $\hat{\boldsymbol{\sigma}}$ and $\tilde{\boldsymbol{\sigma}}$, and the electric displacement tensor, $\hat{\boldsymbol{D}}$, are given by

$$\hat{\boldsymbol{\sigma}}=\boldsymbol{C}:\boldsymbol{\varepsilon}-\boldsymbol{E}\cdot\boldsymbol{e}\quad\equiv\quad\hat{\sigma}_{ij}=C_{ijk\ell}\varepsilon_{k\ell}-E_\ell e_{\ell ij},$$
$$\tilde{\boldsymbol{\sigma}}=\boldsymbol{h}\vdots\boldsymbol{\nabla}\boldsymbol{\varepsilon}-\boldsymbol{E}\cdot\boldsymbol{\mu}\quad\equiv\quad\tilde{\sigma}_{ijk}=h_{ijk\ell mn}\frac{\partial\varepsilon_{\ell m}}{\partial x_n}-E_\ell\mu_{\ell ijk},$$
$$\hat{\boldsymbol{D}}=\boldsymbol{\kappa}\cdot\boldsymbol{E}+\boldsymbol{e}:\boldsymbol{\varepsilon}+\boldsymbol{\mu}\vdots\boldsymbol{\nabla}\boldsymbol{\varepsilon}\quad\equiv\quad\hat{D}_\ell=\kappa_{\ell m}E_m+e_{\ell ij}\varepsilon_{ij}+\mu_{\ell ijk}\frac{\partial\varepsilon_{ij}}{\partial x_k}.$$

In these definitions, $\boldsymbol{\varepsilon}$ is the strain tensor (i.e., $\varepsilon_{ij} = (\partial u_i/\partial x_j + \partial u_j/\partial x_i)/2$), $\boldsymbol{E} = -\boldsymbol{\nabla}\phi$ is the electric field, $\boldsymbol{C}$ is the elasticity tensor (which depends on the Young modulus E and Poisson ratio ν), $\boldsymbol{h}$ is the strain-gradient tensor (defined as $h_{ijk\ell mn} = l^2 C_{ij\ell m}\delta_{kn}$, where l is the internal length scale parameter), $\boldsymbol{e}$ and $\boldsymbol{\mu}$ are the tensors of piezoelectric and flexoelectric coefficients, and $\boldsymbol{\kappa}$ stands for the dielectric permittivity. See appendix B in [8] for detailed definitions.

The physical boundary conditions (3a) set null traction, second traction and surface charge density, defined as

$$t_i(\boldsymbol{u},\phi) := \left(\hat{\sigma}_{ij} - \frac{\partial \tilde{\sigma}_{ijk}}{\partial x_k} - \nabla_k^S \tilde{\sigma}_{ikj}\right) n_j + \tilde{\sigma}_{ijk}\tilde{N}_{jk},$$

$$r_i(\boldsymbol{u},\phi) := \tilde{\sigma}_{ijk} n_j n_k,$$

and

$$w(\boldsymbol{u},\phi) := -\hat{D}_\ell(\boldsymbol{u},\phi) n_\ell,$$

where $\nabla_k^S \tilde{\sigma}_{ikj}$ is the surface divergence of $\tilde{\sigma}_{ikj}$, and $\tilde{N}$ is the second order geometry tensor, see [8] for details. Equation (3b) sets null punctual forces on physical corners, with

$$j_i(\boldsymbol{u},\phi) := \tau_j^L \tilde{\sigma}_{ij\ell}^L n_\ell^L + \tau_j^R \tilde{\sigma}_{ij\ell}^R n_\ell^R, \tag{8}$$

being $\boldsymbol{n}^L$ and $\boldsymbol{n}^R$ the unitary exterior normals on the left and right curves sharing the corner, and $\boldsymbol{\tau}^L$ and $\boldsymbol{\tau}^R$ the unitary tangent vectors on each curve pointing outward; see [8] for details.

The rest of the equations in the problem statement are introduced so that the solution in the unit cell is equivalent to the GP solution in the infinite domain, and we refer to them as GP boundary conditions. Equations (4) impose the solution to be GP functions, with multi-period $\boldsymbol{L} = (L_x, L_y)$, and jumps $\boldsymbol{\Delta}_x^{\boldsymbol{u}} = (\Delta_x^{u_x}, \Delta_x^{u_y})^T$, $\boldsymbol{\Delta}_y^{\boldsymbol{u}} = (\Delta_y^{u_y}, \Delta_y^{u_x})^T$ for the displacement and Δ_x^ϕ, Δ_y^ϕ for the potential.

Remark 2 (Macro-conditions) In practical applications, *macro-conditions* are imposed to deform, or apply a voltage difference, in the unit cell. For each jump variable, we can either set its value, or leave it as an unknown, setting the corresponding dual macroscopic stress or macroscopic charge instead. For instance, in a sensor setting, we can impose a longitudinal macro-strain with magnitude -0.1 in the y direction, by setting $\Delta_y^{u_y}/L_y = -0.1$ and $\Delta_y^{u_x} = \Delta_x^{u_y} = 0$, leaving free, as unknowns, the rest of jumps, and having the potential accumulation Δ_y^ϕ as output of interest, see for instance [17]. The actual expression of the macro-stresses and macro-charges, dual to the jumps, will be deduced from the weak form in section 4.2, and commented in remarks 5 and 6.

Apart from the $\mathcal{C}^0$ continuity of the solution, we must also impose $\mathcal{C}^1$ continuity of the displacement and equilibrium of internal forces on the boundary of the rectangle. The conditions to be imposed are analogous to the conditions imposed on material interfaces, which are the ones imposed also between elements in the C0-IPM method [21].

That is, the $\mathcal{W}$ and $\mathcal{S}$ sides (and also, by geometry periodicity, the $\mathcal{E}$ and $\mathcal{N}$ sides) are artificial interfaces in the infinite domain obtained by repetition of the unit cell. Thus, continuity of the normal derivative of the displacement, equilibrium of first and second tractions and conservation of charge, are imposed in conditions (5), just accounting for the fact that the solution in the unit cell can be repeated in both directions, adding the corresponding constant jumps, and noting that the derivative of a GP function is a periodic function.

Finally, condition (6) for the puntual forces on false corners and on the rectangle corners (if not in a void) are a consequence of the following remark.

Remark 3 If a corner smoothly patches two curves, we have $\boldsymbol{n}^L = \boldsymbol{n}^R$ and $\boldsymbol{\tau}^L = -\boldsymbol{\tau}^R$. Plugging this in (8), for continuous $\tilde{\boldsymbol{\sigma}}$, it can be easily checked that $\boldsymbol{j}(\boldsymbol{u}, \phi) = \boldsymbol{0}$. It would be the case, for instance, for an artificial corner introduced in a smooth curve.

More precisely, by the additional assumptions in section 2.2, false corners are artificial corners, with continuity of the normal vector on the boundary of the infinite domain. Moreover, as noted in remark 1, false corners appear by pairs which are in opposed sides of Ω, either vertically or horizontally aligned. Thus, by remark 3, the punctual forces on the paired false corners must be in equilibrium, summing to zero, as stated in condition (6) for $\mathcal{C}^F$.

Analogously, by replication of the unit cell in the vertical direction, using remark 3, the sum of the punctual forces at the top and bottom corners of the rectangle must be in equilibrium by pairs, i.e. the sum of the forces for the two left corners and the sum for the two right corners is zero. With the same reasoning by repetition in the horizontal direction, we conclude that condition (6) is also satisfied for the rectangle corners $\mathcal{C}^R$.

4 C0-IPM with GP conditions

The C0-IPM formulation for flexoelectricity problems with GP is derived in this section. GP is assumed in both directions, since the reduction to GP in only one direction is straight-forward. The derivations are done in 2D, even though the same methodology can be directly applied in 3D with extra implementation effort.

First, the C0-IPM space is recalled, and it is then modified to accommodate the GP jump conditions in strong form, also stating useful properties of the functions. The weighted residual equations are derived for the mechanical equilibrium equation, and for the electric equation, carefully accounting for the GP conditions. The C0-IPM weak form for the coupled problem is then stated. Finally, the application to the case with GP in only one direction is commented.

4.1 Functional spaces

In the C0-IPM formulation, the domain (in this case the unit cell, Ω) is split in finite elements, $\{\Omega_e\}_{e=1}^{n_{el}}$, and the solution is assumed to be in the space

$$\mathcal{V} := \{v \in \mathcal{H}^1(\Omega) : v \in \mathcal{H}^2(\Omega_e) \text{ for } e = 1, \dots, n_{el}\}.$$

We aim at defining a space, subset of $\mathcal{V}$, fulfilling the GP jump conditions (4). To this end, consider the subset

$$\begin{aligned}\mathcal{V}_L^P := \{v \in \mathcal{V} : v(0,y) = v(L_x,y) \text{ for } (0,y) \in \mathcal{W},\\ v(x,0) = v(x,L_y) \text{ for } (x,0) \in \mathcal{S}\},\end{aligned}$$

corresponding to functions in $\mathcal{V}$ that are periodic in x and y simultaneously, with multi-period $\boldsymbol{L} = (L_x, L_y)$. Now, we consider a pair of functions $\varphi^x \in \mathcal{V}$ and $\varphi^y \in \mathcal{V}$ such that

$$\begin{aligned}\varphi^x(x,0) = \varphi^x(x,L_y),\ \varphi^x(0,y) = 0,\ \varphi^x(L_x,y) = 1,\\ \varphi^y(0,y) = \varphi^y(L_x,y),\ \varphi^y(x,0) = 0,\ \varphi^y(x,L_y) = 1,\end{aligned} \tag{9}$$

(i.e. functions that are periodic in one direction, with unitary jump in the other) and use them to define our GP space $\mathcal{V}_L^{GP} \subset \mathcal{V}$ as

$$\mathcal{V}_L^{GP} := \mathcal{V}_L^P \oplus \langle\varphi^x\rangle \oplus \langle\varphi^y\rangle. \tag{10}$$

In other words, any function $\boldsymbol{w} \in [\mathcal{V}_L^{GP}]^m$ (with m components) can be expressed as

$$\boldsymbol{w} = \boldsymbol{w}^p + \boldsymbol{\Delta}_x^{\boldsymbol{w}}\varphi^x + \boldsymbol{\Delta}_y^{\boldsymbol{w}}\varphi^y, \tag{11}$$

where $\boldsymbol{\Delta}_x^{\boldsymbol{w}} = \boldsymbol{w}(L_x,\cdot) - \boldsymbol{w}(0,\cdot)$ and $\boldsymbol{\Delta}_y^{\boldsymbol{w}} = \boldsymbol{w}(\cdot,L_y) - \boldsymbol{w}(\cdot,0)$ are the constant jumps with the multi-period $\boldsymbol{L} = (L_x, L_y)$, and $\boldsymbol{w}^p = \boldsymbol{w} - \boldsymbol{\Delta}_x^{\boldsymbol{w}}\varphi^x - \boldsymbol{\Delta}_y^{\boldsymbol{w}}\varphi^y \in [\mathcal{V}_L^P]^m$ is a periodic function.

Remark 4 In the light of lemma 1, the natural choice for the functions satisfying (9) is $\varphi^x = x/L_x$ and $\varphi^y = y/L_y$. Nevertheless, in the unit cell Ω, any choice in $\mathcal{V}$ satisfying the conditions (9) leads to the same space $\mathcal{V}_L^{GP}$ and, as commented in remark 8 in section 5, other options may be more convenient.

Some properties of the functions in $\mathcal{V}_L^{GP}$ that will come in handy in the next section are stated next.

Lemma 2 *For $w \in \mathcal{V}_L^{GP}$ and $f : \partial\Omega \to \mathbb{R}$,*

$$\begin{aligned}
&[\![f]\!] = 0 \ \text{ on } \mathcal{W} \ \Rightarrow\ [\![wf]\!](0,y) = \Delta_x^w f(L_x,y) \ \text{ for } (0,y) \in \mathcal{W}\\
&[\![f]\!] = 0 \ \text{ on } \mathcal{S} \ \Rightarrow\ [\![wf]\!](x,0) = \Delta_y^w f(x,L_y) \ \text{ for } (x,0) \in \mathcal{S}\\
&\{f\} = 0 \ \text{ on } \mathcal{W} \Rightarrow\ \{wf\}(0,y) = \tfrac{1}{2}\Delta_x^w f(L_x,y) \ \text{ for } (0,y) \in \mathcal{W}\\
&\{f\} = 0 \ \text{ on } \mathcal{S} \ \Rightarrow\ \{wf\}(x,0) = \tfrac{1}{2}\Delta_y^w f(x,L_y) \ \text{ for } (x,0) \in \mathcal{S}
\end{aligned}$$

Proof We will prove the first statement only, as the proof for the other ones is analogous. Since $w \in \mathcal{V}_L^{GP}$, it can be written as in (11), and

$$\begin{aligned}\llbracket wf \rrbracket(0,y) &= \left[w^p(L_x,y) + \Delta_x^w \varphi^x(L_x,y) + \Delta_y^w \varphi^y(L_x,y)\right] f(L_x,y) \\ &\quad + \left[w^p(0,y) + \Delta_x^w \varphi^x(0,y) + \Delta_y^w \varphi^y(0,y)\right] f(0,y) \\ &= w^p(0,y)\llbracket f \rrbracket + \Delta_y^w \varphi^y(0,y)\llbracket f \rrbracket + \Delta_x^w f(L_x,y) \qquad \text{on } \mathcal{W}.\end{aligned}$$

Thus, using the hypothesis $\llbracket f \rrbracket = 0$ yields the claim. □

Lemma 3 *For $w \in \mathcal{V}_L^{GP}$ and $f \in \mathcal{L}_2(\mathcal{W} \cup \mathcal{E} \cup \mathcal{S} \cup \mathcal{N})$,*

$$\begin{aligned}\llbracket f \rrbracket = 0 \ \text{ on } \mathcal{W} \Rightarrow \int_{\mathcal{W}\cup\mathcal{E}} wf\, d\ell = \Delta_x^w \int_{\mathcal{E}} f\, d\ell, \\ \llbracket f \rrbracket = 0 \ \text{ on } \mathcal{S} \ \Rightarrow \int_{\mathcal{S}\cup\mathcal{N}} wf\, d\ell = \Delta_y^w \int_{\mathcal{N}} f\, d\ell.\end{aligned}$$

Proof Again, we will prove the first statement only. Since the conditions for lemma 2 are met, we have

$$\int_{\mathcal{W}\cup\mathcal{E}} wf \mathrm{d}\ell = \int_{\mathcal{W}} \llbracket wf \rrbracket \mathrm{d}\ell = \Delta_x^w \int_{\mathcal{E}} f \mathrm{d}\ell,$$

as we wanted to show. □

4.2 Weighted residual for the mechanical equilibrium equation

The weighted residual in equation (9) of [21] can be derived from (2a) integrating in each element, applying integration by parts twice and the surface divergence theorem on the integrals involving tangential derivatives of the weighting function $\boldsymbol{v} \in \mathcal{V}$, summing up for all elements, and imposing high-order interface conditions between elements on interior sides, see [21] for details. Here we start from its particularisation for the 2D case, writing it as

$$\begin{aligned}\int_\Omega \boldsymbol{v}\cdot\boldsymbol{b}\,\mathrm{d}\Omega \;=\; &\int_\Omega \boldsymbol{\varepsilon}(\boldsymbol{v}) : \hat{\boldsymbol{\sigma}}(\boldsymbol{u},\phi)\,\mathrm{d}\Omega \;+\; \int_{\widehat{\Omega}} \boldsymbol{\nabla}\boldsymbol{\varepsilon}(\boldsymbol{v}) \dddot{:} \tilde{\boldsymbol{\sigma}}(\boldsymbol{u},\phi)\,\mathrm{d}\Omega \\ &- \int_{\mathcal{I}} \left\llbracket \frac{\partial \boldsymbol{v}}{\partial \boldsymbol{n}} \right\rrbracket \cdot \{\boldsymbol{r}(\boldsymbol{u},\phi)\}\,\mathrm{d}\ell \;-\; \sum_{k=1}^{n_c} \boldsymbol{v}(C_k)\cdot\boldsymbol{J}_k(\boldsymbol{u},\phi) \qquad (12) \\ &- \int_{\partial\Omega} \boldsymbol{v}\cdot\boldsymbol{t}(\boldsymbol{u},\phi)\,\mathrm{d}\ell \;-\; \int_{\partial\Omega} \frac{\partial \boldsymbol{v}}{\partial \boldsymbol{n}}\cdot\boldsymbol{r}(\boldsymbol{u},\phi)\,\mathrm{d}\ell,\end{aligned}$$

where $\mathcal{I}$ is the union of the interior sides of the FE mesh, $\widehat{\Omega} = \Omega \backslash \mathcal{I}$ is the union of the interior of the elements, and the mean and jump operators on $\mathcal{I}$ are defined as usual; that is,

$$\{\boldsymbol{f}\} := (\boldsymbol{f}^L + \boldsymbol{f}^R)/2, \qquad \llbracket \boldsymbol{f} \rrbracket := \boldsymbol{f}^L + \boldsymbol{f}^R \qquad \text{on } \mathcal{I}, \qquad (13)$$

with the indexes L and R referring to the values taken from the left and right elements sharing each side in $\mathcal{I}$.

At the corners of Ω, i.e. $\{C_k\}_{k=1}^{n_c} = \mathcal{C}^R \sqcup \mathcal{C}^F \sqcup \mathcal{C}^T$, $\boldsymbol{J}_k(\boldsymbol{u}, \phi)$ is the sum of the punctual forces from all the elements sharing the corner C_k, see [21]. Assuming that $\tilde{\boldsymbol{\sigma}}(\boldsymbol{u}, \phi)$ is continuous for the analytical solution (which is the case in the absence of material discontinuities or applied external punctual forces), $\boldsymbol{J}_k(\boldsymbol{u}, \phi) = \boldsymbol{j}(\boldsymbol{u}, \phi)|_{C_k}$ defined in (8). Consequently, in equation (12), $\boldsymbol{J}_k(\boldsymbol{u}, \phi)$ has been set to zero on all the element vertexes that are not corners of the domain, because at vertexes in the interior of smooth sides the corner punctual force is zero by remark 3, and at interior vertexes it is null by equilibrium of internal forces, or by simple algebraic cancelation of the sum.

Now, taking $\boldsymbol{u}, \boldsymbol{v} \in [\mathcal{V}_L^{GP}]^2$ and $\phi \in \mathcal{V}_L^{GP}$, we can particularise and simplify the last three terms in (12). First, identifying again the sum of the element corner forces with the punctual force in the domain corner, $\boldsymbol{J}_k(\boldsymbol{u}, \phi) = \boldsymbol{j}(\boldsymbol{u}, \phi)|_{C_k}$, and using that it is null for the physical corners, in $\mathcal{C}^T$, due to the homogeneous physical boundary condition (3b), we have

$$\sum_{k=1}^{n_c} \boldsymbol{v}(C_k) \cdot \boldsymbol{J}_k(\boldsymbol{u}, \phi) = \sum_{C_k \in \mathcal{C}^R \cup \mathcal{C}^R} \boldsymbol{v}(C_k) \cdot \boldsymbol{j}(\boldsymbol{u}, \phi)|_{C_k}.$$

Now, expanding $\boldsymbol{v} \in \mathcal{V}_L^{GP}$ as in (11), evaluating the sum at the four corners of the rectangle, and using the properties (9), it is easy to check that

$$\begin{aligned}\sum_{C_k \in \mathcal{C}^R} \boldsymbol{v}(C_k) \cdot \boldsymbol{j}(\boldsymbol{u}, \phi)|_{C_k} &= \boldsymbol{\Delta}_x^{\boldsymbol{v}} \left[\boldsymbol{j}(\boldsymbol{u}, \phi)|_{(L_x,0)} + \boldsymbol{j}(\boldsymbol{u}, \phi)|_{(L_x,L_y)}\right] \\ &\quad + \boldsymbol{\Delta}_y^{\boldsymbol{v}} \left[\boldsymbol{j}(\boldsymbol{u}, \phi)|_{(0,L_y)} + \boldsymbol{j}(\boldsymbol{u}, \phi)|_{(L_x,L_y)}\right] \\ + \boldsymbol{v}^p(0,0) \left[\boldsymbol{j}(\boldsymbol{u}, \phi)|_{(0,0)} + \boldsymbol{j}(\boldsymbol{u}, \phi)|_{(L_x,0)}\right. &\left. + \boldsymbol{j}(\boldsymbol{u}, \phi)|_{(0,L_y)} + \boldsymbol{j}(\boldsymbol{u}, \phi)|_{(L_x,L_y)}\right].\end{aligned}$$

Thus, applying the GP conditions on the rectangle corners (6), the sum is

$$\sum_{C_k \in \mathcal{C}^R} \boldsymbol{v}(C_k) \cdot \boldsymbol{j}(\boldsymbol{u}, \phi)|_{C_k} = 0.$$

Now, due to remark 1, the corners in $\mathcal{C}^F$ appear by pairs that are in opposed sides, vertically or horizontally aligned. Thus, the total summation over the corners can be expressed as

$$\sum_{k=1}^{n_c} \boldsymbol{v}(C_k) \cdot \boldsymbol{J}_k(\boldsymbol{u}, \phi) = 2 \sum_{C_k \in \mathcal{C}^F \cap (\overline{\mathcal{W}} \cup \overline{\mathcal{S}})} \{\boldsymbol{v} \cdot \boldsymbol{j}(\boldsymbol{u}, \phi)\}|_{C_k}.$$

Moreover, using the GP material interface condition (6) on the false corners, the hypothesis of lemma 2 are met, and the sum can be written as

$$\sum_{k=1}^{n_c} \boldsymbol{v}(C_k) \cdot \boldsymbol{J}_k(\boldsymbol{u}, \phi) = \boldsymbol{\Delta}_x^{\boldsymbol{v}} \cdot \sum_{C_k \in \mathcal{C}^F \cap \overline{\mathcal{E}}} \boldsymbol{j}(\boldsymbol{u}, \phi)|_{C_k} + \boldsymbol{\Delta}_y^{\boldsymbol{v}} \cdot \sum_{C_k \in \mathcal{C}^F \cap \overline{\mathcal{N}}} \boldsymbol{j}(\boldsymbol{u}, \phi)|_{C_k}. \quad (14)$$

We now focus on the first boundary integral in equation (12), which involves the first traction force $\boldsymbol{t}$. Splitting the boundary, the integral can be decomposed in three integrals: on $\mathcal{E} \cup \mathcal{W}$, on $\mathcal{S} \cup \mathcal{N}$ and on $\partial\Omega^i$, respectively. Due to the GP material interface conditions on the traction (5), the conditions of lemma 3 are met, and the integrals on $\mathcal{E} \cup \mathcal{W}$ and $\mathcal{S} \cup \mathcal{N}$ simplify accordingly. Moreover, due to the homogeneous first Neumann boundary condition (3a), the integral on $\partial\Omega^i$ vanishes. Thus, we conclude

$$\int_{\partial\Omega} \boldsymbol{v} \cdot \boldsymbol{t}(\boldsymbol{u}, \phi) \mathrm{d}\ell = \boldsymbol{\Delta}_x^{\boldsymbol{v}} \cdot \int_{\mathcal{E}} \boldsymbol{t}(\boldsymbol{u}, \phi) \mathrm{d}\ell + \boldsymbol{\Delta}_y^{\boldsymbol{v}} \cdot \int_{\mathcal{N}} \boldsymbol{t}(\boldsymbol{u}, \phi) \mathrm{d}\ell. \tag{15}$$

It only remains to tackle the second boundary integral in equation (12). Splitting the boundary again and using the second homogeneous Neumann boundary condition (3a), the integral can be written as

$$\int_{\partial\Omega} \frac{\partial \boldsymbol{v}}{\partial \boldsymbol{n}} \cdot \boldsymbol{r}(\boldsymbol{u}, \phi) \, \mathrm{d}\ell = \int_{\mathcal{S}\cup\mathcal{W}} \left[\!\!\left[\frac{\partial \boldsymbol{v}}{\partial \boldsymbol{n}} \cdot \boldsymbol{r}(\boldsymbol{u}, \phi) \right]\!\!\right] \, \mathrm{d}\ell.$$

Now we recall a well-known identity in the context of interfaces or element sides: $[\![ab\boldsymbol{n}]\!] = \{a\}[\![b\boldsymbol{n}]\!] + [\![a\boldsymbol{n}]\!]\{b\}$. Applying it on the artificial boundaries, $\mathcal{S}$ and $\mathcal{W}$, and using the GP condition for $\boldsymbol{r}$ in (5), the integral becomes

$$\int_{\partial\Omega} \frac{\partial \boldsymbol{v}}{\partial \boldsymbol{n}} \cdot \boldsymbol{r} \, \mathrm{d}\ell = \int_{\mathcal{S}\cup\mathcal{W}} \left[\!\!\left[\frac{\partial \boldsymbol{v}}{\partial \boldsymbol{n}} \right]\!\!\right] \cdot \{\boldsymbol{r}(\boldsymbol{u}, \phi)\} \, \mathrm{d}\ell. \tag{16}$$

Finally, plugging results (14), (15), and (16) into equation (12), we obtain the weighted residual for the mechanical equilibrium equation with GP:

$$\begin{aligned} \int_{\Omega} \boldsymbol{v} \cdot \boldsymbol{b} \, \mathrm{d}\Omega = & \int_{\Omega} \boldsymbol{\varepsilon}(\boldsymbol{v}) : \hat{\boldsymbol{\sigma}}(\boldsymbol{u}, \phi) \, \mathrm{d}\Omega + \int_{\widehat{\Omega}} \boldsymbol{\nabla}\boldsymbol{\varepsilon}(\boldsymbol{v}) \dddot{:} \tilde{\boldsymbol{\sigma}}(\boldsymbol{u}, \phi) \, \mathrm{d}\Omega \\ & - \int_{\mathcal{I}\cup\mathcal{S}\cup\mathcal{W}} \left[\!\!\left[\frac{\partial \boldsymbol{v}}{\partial \boldsymbol{n}} \right]\!\!\right] \cdot \{\boldsymbol{r}(\boldsymbol{u}, \phi)\} \, \mathrm{d}\ell - \boldsymbol{\Delta}_y^{\boldsymbol{v}} \cdot \boldsymbol{F}_y(\boldsymbol{u}, \phi) - \boldsymbol{\Delta}_x^{\boldsymbol{v}} \cdot \boldsymbol{F}_x(\boldsymbol{u}, \phi), \end{aligned} \tag{17}$$

with

$$\begin{aligned} \boldsymbol{F}_x(\boldsymbol{u}, \phi) &:= \sum_{C_k \in \mathcal{C}^F \cap \overline{\mathcal{E}}} \boldsymbol{j}(\boldsymbol{u}, \phi)|_{C_k} + \int_{\mathcal{E}} \boldsymbol{t}(\boldsymbol{u}, \phi) \mathrm{d}\ell, \\ \boldsymbol{F}_y(\boldsymbol{u}, \phi) &:= \sum_{C_k \in \mathcal{C}^F \cap \overline{\mathcal{N}}} \boldsymbol{j}(\boldsymbol{u}, \phi)|_{C_k} + \int_{\mathcal{N}} \boldsymbol{t}(\boldsymbol{u}, \phi) \mathrm{d}\ell. \end{aligned} \tag{18}$$

Remark 5 (Macro-stresses) $\boldsymbol{F}_x$ and $\boldsymbol{F}_y$ in (18) are the sum of the forces on the $\mathcal{E}$ and $\mathcal{N}$ sides, respectively, including both traction forces and corner punctual forces. In fact, $\boldsymbol{F}_x/L_y$ and $\boldsymbol{F}_y/L_x$ can be interpreted as macroscopic stresses applied to the metamaterial in the macro scale, since they are the dual quantities of the imposed macro-strains given by $\Delta_x^{\boldsymbol{u}}/L_x$ and $\Delta_y^{\boldsymbol{u}}/L_y$, see [17]. The macro-conditions can then be either setting the jump (Dirichlet) or the corresponding force (Neumann), for each component of the displacement and for each direction.

In all the examples in this manuscript, the loading is always done by setting some jumps, and homogeneous Neumann macro-conditions are assumed otherwise. As an example, if we set $\Delta_x^{\boldsymbol{u}} = (-0.1L_x, 0)^T$, and let free the rest of jumps, then the mechanical Neumann macro-condition is $\boldsymbol{F}_y(\boldsymbol{u}, \phi) = \boldsymbol{0}$. In this case, the weighting function $\boldsymbol{v}$ satisfies $\Delta_x^{\boldsymbol{v}} = 0$, which is the homogeneous version of the Dirichlet macro-condition. In any case, $\boldsymbol{\Delta}_y^{\boldsymbol{v}} \cdot \boldsymbol{F}_y(\boldsymbol{u}, \phi) + \boldsymbol{\Delta}_x^{\boldsymbol{v}} \cdot \boldsymbol{F}_x(\boldsymbol{u}, \phi) = 0$ holds. Thus, the weighted residual (17), valid for $\boldsymbol{u} \in [\mathcal{V}_L^{GP}]^2$ and $\phi \in \mathcal{V}_L^{GP}$, reduces to

$$\int_\Omega \boldsymbol{v} \cdot \boldsymbol{b} \, \mathrm{d}\Omega = \int_\Omega \boldsymbol{\varepsilon}(\boldsymbol{v}) : \hat{\boldsymbol{\sigma}}(\boldsymbol{u}, \phi) \, \mathrm{d}\Omega + \int_{\widehat{\Omega}} \boldsymbol{\nabla}\boldsymbol{\varepsilon}(\boldsymbol{v}) \dddot{:} \tilde{\boldsymbol{\sigma}}(\boldsymbol{u}, \phi) \, \mathrm{d}\Omega - \int_{\mathcal{I}\cup\mathcal{S}\cup\mathcal{W}} \left[\!\!\left[\frac{\partial \boldsymbol{v}}{\partial \boldsymbol{n}} \right]\!\!\right] \cdot \{\boldsymbol{r}(\boldsymbol{u}, \phi)\} \, \mathrm{d}\ell \quad (19)$$

for any $\boldsymbol{v} \in [\mathcal{V}_L^{GP}]^2$ satisfying the Dirichlet macro-conditions in homogeneous form.

4.3 Weighted residual for the electric displacement equation

We now derive the weighted residual for the PDE (2b). Multiplying it by a test function $\nu \in \mathcal{V}_L^{GP}$, integrating over Ω, resourcing to integration by parts, and using the definition of the electric charge density, w, we get

$$\int_\Omega \boldsymbol{\nabla}\nu \cdot \hat{\boldsymbol{D}}(\boldsymbol{u}, \phi) \, \mathrm{d}\Omega = -\int_\Omega \nu q \, \mathrm{d}\Omega + \int_{\partial\Omega} \nu w(\boldsymbol{u}, \phi) \, \mathrm{d}\ell.$$

Like before, we address the integral on $\partial\Omega$ splitting it in three integrals, on $\mathcal{E} \cup \mathcal{W}$, on $\mathcal{S} \cup \mathcal{N}$ and on $\partial\Omega^i$, respectively. Due to the GP material interface conditions for the electric charge density in (5), the conditions of lemma 3 are met, and the integrals on $\mathcal{E}\cup\mathcal{W}$ and $\mathcal{S}\cup\mathcal{N}$ simplify accordingly. Moreover, due to the homogeneous physical boundary condition (3a) on the charge density, w, the integral on $\partial\Omega^i$ vanishes, and so we conclude

$$\int_\Omega \boldsymbol{\nabla}\nu \cdot \hat{\boldsymbol{D}}(\boldsymbol{u}, \phi) \, \mathrm{d}\Omega = -\int_\Omega \nu q \, \mathrm{d}\Omega - \Delta_x^\nu Q_x - \Delta_y^\nu Q_y.$$

with

$$Q_x := -\int_{\mathcal{E}} w(\boldsymbol{u}, \phi) \mathrm{d}\ell, \qquad Q_y := -\int_{\mathcal{N}} w(\boldsymbol{u}, \phi) \mathrm{d}\ell. \quad (20)$$

Remark 6 (Macro-charges) Q_x and Q_y in (20) are the total electric charges in the $\mathcal{E}$ and $\mathcal{N}$ sides, respectively. In fact, Q_x/L_y and Q_y/L_x can be interpreted as macroscopic electric displacements applied to the metamaterial in the macro scale, since they are the dual quantities of the imposed macroscopic electric fields given by $-\Delta_x^\phi/L_x$ and $-\Delta_y^\phi/L_y$. The macro-conditions can then be either setting the jump (Dirichlet) or the corresponding charge (Neumann), for each direction.

As we did for the weighted residual for the displacements, for each one of the spatial directions, we either impose a jump of the potential, or leave it free with an homogeneous Neumann macro-condition. For example, if we impose Δ_x^ϕ to some given value to apply a voltage difference, the rest of macro-conditions are homogeneous Neumann, that is, $Q_y = 0$. Thus, in any case, the weighted residual equation for the electric potential reduces to the standard one,

$$\int_\Omega \boldsymbol{\nabla}\nu \cdot \hat{\boldsymbol{D}}(\boldsymbol{u},\phi)\,\mathrm{d}\Omega = -\int_\Omega \nu q\,\mathrm{d}\Omega, \tag{21}$$

and it holds for any $\nu \in \mathcal{V}_L^{GP}$ satisfying the homogeneous version of the Dirichlet macro-conditions.

4.4 Weak form

We can now state the C0-IPM weak form with GP conditions, from the weighted residual equations (19) and (21), following the standard procedure, as in [21]. That is, we sum both equations, and we add terms to symmetrise the weak form and to recover the coercivity of the strain-gradient elasticity bilinear form.

For the sake of clarity, we will state the weak form for a particular case of macro-conditions, imposing a compression in the horizontal direction, with $\Delta_x^{\boldsymbol{u}}/L_x = (-0.1, 0)^T$, and letting free all other jumps, with homogeneous Neumann macro-conditions, i.e. $Q_x = Q_y = 0$ and $\boldsymbol{F}_y = \boldsymbol{0}$.

The weak form is then: find $\phi \in \mathcal{V}_L^{GP}$ and $\boldsymbol{u} \in [\mathcal{V}_L^{GP}]^2$ such that

$$\Delta_x^{\boldsymbol{u}} = L_x \begin{bmatrix} -0.1 \\ 0 \end{bmatrix} \tag{22}$$

and

$$\begin{aligned}\int_\Omega \boldsymbol{\varepsilon}(\boldsymbol{v}) : \hat{\boldsymbol{\sigma}}(\boldsymbol{u},\phi)\,\mathrm{d}\Omega + \int_{\widehat{\Omega}} \boldsymbol{\nabla}\boldsymbol{\varepsilon}(\boldsymbol{v}) \dddot{:} \tilde{\boldsymbol{\sigma}}(\boldsymbol{u},\phi)\,\mathrm{d}\Omega + \int_\Omega \boldsymbol{\nabla}\nu \cdot \hat{\boldsymbol{D}}(\boldsymbol{u},\phi)\,\mathrm{d}\Omega \\ - \int_{\mathcal{I}\cup\mathcal{S}\cup\mathcal{W}} \left[\!\left[\frac{\partial \boldsymbol{v}}{\partial \boldsymbol{n}}\right]\!\right] \cdot \{\boldsymbol{r}(\boldsymbol{u},\phi)\}\,\mathrm{d}\ell - \int_{\mathcal{I}\cup\mathcal{S}\cup\mathcal{W}} \{\boldsymbol{r}(\boldsymbol{v},\nu)\} \cdot \left[\!\left[\frac{\partial \boldsymbol{u}}{\partial \boldsymbol{n}}\right]\!\right] \mathrm{d}\ell \\ + \int_{\mathcal{I}\cup\mathcal{S}\cup\mathcal{W}} \beta \left[\!\left[\frac{\partial \boldsymbol{v}}{\partial \boldsymbol{n}}\right]\!\right] \cdot \left[\!\left[\frac{\partial \boldsymbol{u}}{\partial \boldsymbol{n}}\right]\!\right] \mathrm{d}\ell = \int_\Omega \boldsymbol{v}\cdot\boldsymbol{b}\,\mathrm{d}\Omega - \int_\Omega \nu q\,\mathrm{d}\Omega \end{aligned} \tag{23}$$

for all $\nu \in \mathcal{V}_L^{GP}$ and $\boldsymbol{v} \in [\mathcal{V}_L^{GP}]^2$ such that $\Delta_x^{\boldsymbol{v}} = \boldsymbol{0}$, where the jump and mean operators are defined in (13) for the interior element sides in $\mathcal{I}$, and in (7) for the artificial boundaries $\mathcal{S}\cup\mathcal{W}$.

In (23), the term $-\int_{\mathcal{I}\cup\mathcal{S}\cup\mathcal{W}} \{\boldsymbol{r}(\boldsymbol{v},\nu)\} \cdot \left[\!\left[\frac{\partial \boldsymbol{u}}{\partial \boldsymbol{n}}\right]\!\right] \mathrm{d}\ell$ is added to recover the symmetry of the weak form. It is analytically zero, since $\left[\!\left[\frac{\partial \boldsymbol{u}}{\partial \boldsymbol{n}}\right]\!\right] = 0$ on $\mathcal{E}\cup\mathcal{N}$ due to the first GP interface conditions in (5), and on $\mathcal{I}$ due to the assumed $\mathcal{C}^1$ continuity of the analytical solution $\boldsymbol{u}$ in the interior of Ω. The integral $\int_{\mathcal{I}\cup\mathcal{S}\cup\mathcal{W}} \beta \left[\!\left[\frac{\partial \boldsymbol{v}}{\partial \boldsymbol{n}}\right]\!\right] \cdot \left[\!\left[\frac{\partial \boldsymbol{u}}{\partial \boldsymbol{n}}\right]\!\right] \mathrm{d}\ell$, also null for the analytical solution for the same

reason, provides coercivity of the strain-gradient elasticity bilinear form, for large enough stabilization parameter β. This parameter can be estimated solving an eigenvalue problem, see [21] for details. In the numerical examples, we use $\beta = 1$ if $l = 0$, since any $\beta > 0$ is valid in this case, and $\beta = 100El^2/h$, otherwise.

It is worth noting the homogeneous version of the Dirichlet macro-condition imposed on the weighting function, $\Delta_x^{\boldsymbol{v}} = \mathbf{0}$, associated to the condition (22) on the displacement, and recalling that homogeneous Neumann macro-conditions are assumed for free jumps.

As a second example, in the so-called sensor setting we would impose a jump on the potential, $\Delta_x^{\phi} = V$, and the condition on the weighting functions would be in this case, its homogeneous version, $\Delta_x^{\nu} = 0$.

Remark 7 The weak form stated in this section does not have a unique solution, since it is determined up to a constant for the potential, and rigid-body-motion displacements. To have a unique solution, we prescribe the potential and the displacement at one node, to set the constant for the potential and to preclude rigid translations. Rigid rotations can be precluded imposing $\Delta_y^{u_x} = \Delta_x^{u_y}$ as in [17], although a unique solution is also obtained if the jump $\Delta_x^{u_y}$, or $\Delta_y^{u_x}$, is set. The same applies for GP in only one direction if Neumann boundary conditions are applied on the physical boundaries.

4.5 GP in one direction

As previously mentioned, following the same rationale, the C0-IPM weak form can be easily derived for the case with GP in only one direction. In this case, the integrals involving means and jumps restrict only to interior sides and the GP boundary and, if non-homogeneous boundary conditions are imposed on the physical boundary, some terms have to be added to the weak form, to account for them as in the stardard case [21].

More precisely, if GP is assumed in the x-direction, the integrals in (23) restrict to $\mathcal{I} \cup \mathcal{W}$, and we should add to the right-hand-side

$$s(\boldsymbol{v}, \nu) = \int_{\Gamma_{N_1}^{\boldsymbol{u}}} \boldsymbol{v} \cdot \boldsymbol{t}_n \, d\ell + \int_{\Gamma_{N_2}^{\boldsymbol{u}}} \frac{\partial \boldsymbol{v}}{\partial \boldsymbol{n}} \cdot \boldsymbol{r}_n \, d\ell + \sum_{C_k \in \Gamma_{N_1}^{\boldsymbol{u}}} \boldsymbol{v}(C_k) \cdot \boldsymbol{j}^{ext}(C_k) - \int_{\Gamma_{N_1}^{\phi}} \nu w_n \, d\ell$$

if the physical boundary conditions are $\boldsymbol{t}_n(\boldsymbol{u}, \phi) = \boldsymbol{t}_n$ on $\Gamma_{N_1}^{\boldsymbol{u}}$, $\boldsymbol{r}(\boldsymbol{u}, \phi) = \boldsymbol{r}_n$ on $\Gamma_{N_2}^{\boldsymbol{u}}$, $\boldsymbol{j}(\boldsymbol{u}, \phi) = \boldsymbol{j}^{ext}$ on the corners in $\Gamma_{N_1}^{\boldsymbol{u}}$, and $w(\boldsymbol{u}, \phi) = w_n$ on $\Gamma_{N_1}^{\phi}$, with $\Gamma_{N_1}^{\boldsymbol{u}}, \Gamma_{N_2}^{\boldsymbol{u}}, \Gamma_{N_1}^{\boldsymbol{u}} \subseteq \mathcal{S} \cup \mathcal{N}$

First Dirichlet boundary conditions (i.e. prescribed values of the displacement or the potential) can be imposed directly setting the corresponding nodal values. And, although they are usually not considered in realistic applications, Nitsche's method could be used to weakly impose second Dirichlet boundary conditions on the displacement (i.e. conditions on the normal derivative), as usual in standard C0-IPM methods.

5 Implementation of C0-IPM with GP based on nodal FE basis functions

In this section, we present a methodology to implement generalised periodicity in the context of the FE method, which is applicable to any kind of PDE. First we define the approximation space for the GP space, $\mathcal{V}_L^{GP}$, in terms of the standard nodal basis of the FE discretization. Then, given the system in the standard nodal basis (in this case, the system for standard C0-IPM), we detail how to reduce the system to the GP approximation space. Finally, we add some comments on the complete implementation of the C0-IPM method with GP.

5.1 Approximation space with GP

As mentioned before, the unit cell $\Omega \subset \mathbb{R}^2$ is split in elements $\{\Omega_e\}_{e=1}^{n_{el}}$, and, as usual in FE methods, a $\mathcal{C}^0$ element-by-element piecewise polynomial approximation is considered. The nodes of the FE mesh are denoted by $\{\boldsymbol{x}_i\}_{i=1}^{n_{nod}}$. We denote by C the ordered set of the indexes of the nodes corresponding to the 0 or 4 corners of the rectangle; by W, E, S, N the indexes of the nodes on the sides $\overline{\mathcal{W}}$, $\overline{\mathcal{E}}$, $\overline{\mathcal{S}}$ and $\overline{\mathcal{N}}$, respectively, not including the rectangle corners; and by Z the set for the rest of the nodes.

Then, to simplify the implementation, we will assume that the ordering of the nodes is such that

$$C < W < E < S < N < Z,$$

where two sets A and B are said to be $A < B$ if $a_i < b_j$ for all $a_i \in A$ and $b_j \in B$.

In addition, we will assume that the nodes on opposite sides of the domain are horizontally or vertically aligned in pairs. That is,

$$\{x_i \,:\, (x_i, 0) \in \overline{\mathcal{S}}\} = \{x_i \,:\, (x_i, L_y) \in \overline{\mathcal{N}}\}$$
$$\{y_i \,:\, (0, y_i) \in \overline{\mathcal{W}}\} = \{y_i \,:\, (L_x, y_i) \in \overline{\mathcal{E}}\},$$

and we will denote by π and τ the permutations from one side to its opposite side, in the horizontal and vertical directions, respectively. That is,

$$y_i = y_{\pi(i)} \quad \text{for } i \in W, \qquad x_i = x_{\tau(i)} \quad \text{for } i \in S.$$

Now, let us denote by $\{N_i\}_{i=1}^{n_{nod}}$ the standard FE basis functions. We aim at finding a basis satisfying GP jump conditions in both directions. The case with GP only in the horizontal or vertical direction can be derived analogously.

Consider a scalar function u in the FE space,

$$u(\boldsymbol{x}) = \sum_{i=1}^{n_{nod}} u_i N_i(\boldsymbol{x}), \tag{24}$$

complying with the GP jump conditions with multi-period $\boldsymbol{L} = (L_x, L_y)$, that is

$$u(L_x, y) = u(0, y) + \Delta_x^u \quad u(x, L_y) = u(x, 0) + \Delta_y^u.$$

Then, its nodal values satisfy

$$u_{\pi(i)} = u_i + \Delta_x^u \quad \text{for } i \in W, \qquad u_{\tau(j)} = u_j + \Delta_y^u \quad \text{for } i \in S. \tag{25}$$

In addition, if the corners are not in a void, the values at the four corners can be expressed in terms of one corner as

$$u_{SE} = u_{SW} + \Delta_x^u, \quad u_{NW} = u_{SW} + \Delta_y^u, \quad u_{NE} = u_{SW} + \Delta_x^u + \Delta_y^u, \tag{26}$$

where SW, SE, NW and NE denote the indexes of the nodes for the bottom-left, bottom-right, top-left and top-right corners of the rectangle, respectively.

Thus, if the corners are not in a void, the function $u \in \mathcal{V}_L^{GP}$ can be expressed as

$$\begin{aligned} u = \sum_{i\in Z} u_i N_i + \sum_{i\in W} u_i[N_i + N_{\pi(i)}] + \sum_{i\in S} u_i[N_i + N_{\tau(i)}] \\ + u_{SW}[N_{SW} + N_{SE} + N_{NE} + N_{NW}] + \\ + \Delta_x^u \left[N_{SE} + N_{NE} + \sum_{i\in E} N_i \right] + \Delta_y^u \left[N_{NE} + N_{NW} + \sum_{i\in N} N_i \right], \end{aligned}$$

and the approximation space with GP jump conditions is $< \hat{N}_i >_{i=1}^{n_{GP}}$ with

$$\hat{\boldsymbol{N}} = \begin{bmatrix} \hat{N}_1 \\ \hat{N}_2 \\ \hat{N}_3 \\ \hat{N}_{3+1} \\ \vdots \\ \hat{N}_{3+|W|} \\ \hat{N}_{r+1} \\ \vdots \\ \hat{N}_{r+|S|} \\ \hat{N}_{r+|S|+1} \\ \vdots \\ \hat{N}_{n_{GP}} \end{bmatrix} := \begin{bmatrix} N_{SE} + N_{NE} + \sum_{i\in E} N_i \\ N_{NE} + N_{NW} + \sum_{i\in N} N_i \\ N_{SW} + N_{SE} + N_{NW} + N_{NE} \\ N_{4+1} + N_{\pi(4+1)} \\ \vdots \\ N_{4+|W|} + N_{\pi(4+|W|)} \\ N_{s+1} + N_{\pi(s+1)} \\ \vdots \\ N_{s+|S|} + N_{\pi(s+|S|)} \\ N_{s+|S|+|N|+1} \\ \vdots \\ N_{n_{nod}} \end{bmatrix}, \tag{27}$$

$r = 3 + |W|$, $s = 4 + 2|W|$ and $n_{GP} = 3 + |W| + |S| + |Z|$.

If the corners of the rectangle are in a void, $\hat{N}_3$ is not included in the basis, $\hat{N}_1 = \sum_{i\in E} N_i$, and $\hat{N}_2 = \sum_{i\in N} N_i$.

In any case, the new basis can be expressed in terms of the standard one as

$$\hat{\boldsymbol{N}}(x) = \mathbf{P}\boldsymbol{N}(x) \tag{28}$$

with a matrix $\mathbf{P} \in \mathbb{R}^{n_{GP} \times n_{nod}}$, whose non-null coefficients are ones in the proper locations, see details in [2].

Remark 8 The coefficients corresponding to the first two basis functions in (27) are the jumps in each direction, Δ_x^u and Δ_y^u. These two basis functions are in fact particular cases of the functions φ^x and φ^y satisfying (9). The rest of the functions in the basis are periodic in both directions, altogether generating an approximation space for $\mathcal{V}_L^{GP}$ as defined in (10).

We can also express the coefficients of the approximation in the GP space $\{\hat{u}_i\}_{i=1}^{n_{GP}}$ (i.e. the nodal values for $\boldsymbol{x}_i \in [0, L_x) \times [0, L_y)$ and the jumps Δ_x^u and Δ_y^u) in terms of the nodal values in the standard FE space, $\{u_i\}_{i=1}^{n_{nod}}$. Indeed, $u \in \mathcal{V}^{GP} \cap < N_i >_{i=1}^{n_{nod}} = < \hat{N}_i >_{i=1}^{n_{GP}}$ can uniquely be expressed in both spaces as (24) or as

$$u(\boldsymbol{x}) = \sum_{i=1}^{n_{GP}} \hat{u}_i \hat{N}_i(\boldsymbol{x}), \tag{29}$$

which in vector form reads

$$u(\boldsymbol{x}) = \boldsymbol{N}^T(x)\mathbf{u} = \hat{\boldsymbol{N}}^T(x)\hat{\mathbf{u}}.$$

Replacing now (28) we deduce that $\boldsymbol{N}^T(\boldsymbol{x})\mathbf{u} = \boldsymbol{N}^T(\boldsymbol{x})\mathbf{P}^T\hat{\mathbf{u}}$ for any $\boldsymbol{x} \in \mathbb{R}^n$. Thus, the coefficients in both basis are related by

$$\mathbf{u} = \mathbf{P}^T\hat{\mathbf{u}}. \tag{30}$$

5.2 System reduction

Let us assume now that we have the system of equations corresponding to the discretization of the PDEs without Dirichlet or GP conditions. In our application of interest, this is the matrix $\mathbf{K}$ and the right-hand-side $\mathbf{f}$, that we would obtain with a function implementing the standard C0-IPM method for flexoelectricity, such that

$$\mathbf{w}^T\mathbf{K}\mathbf{x} = \mathbf{w}^T\mathbf{f} \quad \forall\, \mathbf{w} \in \mathbb{R}^{3n_{nod}}, \qquad \text{with } \mathbf{x} = \begin{bmatrix} \mathbf{u}^1 \\ \mathbf{u}^2 \\ \boldsymbol{\phi} \end{bmatrix}, \tag{31}$$

being $\mathbf{u}^1$, $\mathbf{u}^2$ and $\boldsymbol{\phi}$ the nodal values of the components of the displacement and of the potential, in the standard FE nodal basis. Assuming now that the displacement and the potential approximations are in the GP space, from (30) we know that the coefficients, $\hat{\mathbf{x}}$ and $\hat{\mathbf{w}}$, of the solution and the weighting functions in the basis with GP ((27) in the case of GP in both directions) satisfy

$$\mathbf{x} = \mathbf{Q}^T\hat{\mathbf{x}}, \quad \mathbf{w} = \mathbf{Q}^T\hat{\mathbf{w}} \quad \text{with } \mathbf{Q} = \begin{bmatrix} \mathbf{P} & & \\ & \mathbf{P} & \\ & & \mathbf{P} \end{bmatrix}.$$

Replacing in (31) we get

$$\hat{\mathbf{w}}^T\mathbf{Q}\mathbf{K}\mathbf{Q}^T\hat{\mathbf{x}} = \hat{\mathbf{w}}^T\mathbf{Q}\mathbf{f}, \quad \forall\, \hat{\mathbf{w}}^T \in \mathbb{R}^{3n_{GP}}.$$

Thus, the system in the reduced GP space is

$$\hat{\mathbf{K}}\hat{\mathbf{x}} = \hat{\mathbf{f}} \quad \text{with } \hat{\mathbf{K}} = \mathbf{Q}\mathbf{K}\mathbf{Q}^T, \quad \hat{\mathbf{f}} = \mathbf{Q}\mathbf{f}$$

5.3 Steps to implement GP conditions in a C0-IPM FE code

In the light of the previous sections, given a function that implements the standard C0-IPM, the implementation of the C0-IPM system with GP is straightforward. The steps to follow are:

1. Adding the sides on the boundary of the rectangle to the list of interior sides.
2. Computing the matrix, $\mathbf{K}$, and the right-hand-side vector, $\mathbf{f}$, with the standard C0-IPM function, and the modified list of interior sides.
3. Reducing the matrix and the right-hand-side vector to the GP approximation space, as explained in sections 5.1 and 5.2.
4. Imposing macro-conditions by setting the coefficients of the approximation (29) corresponding to the jumps to be prescribed, and also prescribe the displacement and the potential at one node (if GP is applied in both directions, or GP is assumed in one direction and homogeneous Neumann conditions are considered on the physical boundary), to preclude rigid body motions and set the constant of the potential. It can be implemented as usually done for Dirichlet boundary conditions in the FE method.
5. Solving the linear system to obtain the coefficients of the solution in the GP basis, $\hat{\mathbf{x}}$, including also the nodal values of the displacement and the potential set in step 4.
6. Building the vector of nodal values in the standard FE basis, $\mathbf{x} = \mathbf{Q}^T\hat{\mathbf{x}}$, to include the rectangle corners and the rest of nodes on $\overline{\mathcal{E}}$ and $\overline{\mathcal{W}}$, satisfying the GP jump conditions (25) and (26).

In the first and second step, horizontally, we conceptually identify the mesh sides on $\mathcal{W}$ and $\mathcal{E}$, and we add this sides to the list of interior sides, taking the element including the side in $\mathcal{W}$ as right element and the element including the twin side in $\mathcal{E}$ as left element. We proceed in the same way vertically. In this way, the integrals involving jumps and means on $\mathcal{I}$ in the standard C0-IPM method now include also the integrals on $\mathcal{W} \cup \mathcal{S}$ to adapt to the GP weak form (23) with the extended definition of the jump and mean operators on the artificial boundaries (7). The first two steps of the procedure account then for the weak imposition of the GP conditions corresponding to equilibrium of tractions and high-order artificial interface conditions in equations (5) and (6).

Steps from 3 to 6 take care of the implementation of the GP jump conditions (4) and the Dirichlet macro-conditions.

6 Numerical experiments

6.1 Convergence tests with a synthetic solution

In this section we perform a convergence test with a synthetic problem in the rectangle $\Omega = [0, L_x] \times [0, L_y]$, with $L_x = 2$ and $L_y = 1$, and with a circular perforation of radii 0.25 in its centre. Figure 5 shows the coarsest mesh used in the test, with triangular elements of degree $p = 3$.

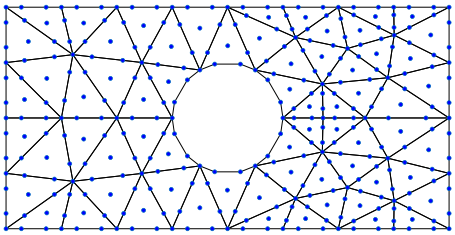

Fig. 5 Coarsest mesh used in the convergence test, with triangular elements of degree $p = 3$.

All the data is defined so that the analytical solution is

$$\begin{aligned} u_x(x,y) &= \sin\left(2\pi(x+y)\right) + x\Delta_x^{u_x}/L_x + y\Delta_y^{u_x}/L_y, \\ u_y(x,y) &= \cos\left(2\pi(x+y)\right) + x\Delta_x^{u_y}/L_x + y\Delta_y^{u_y}/L_y, \\ \phi(x,y) &= \sin\left(2\pi(x+y)\right) + \cos\left(2\pi(x+y)\right) + x\Delta_x^{\phi}/L_x + y\Delta_y^{\phi}/L_y, \end{aligned} \tag{32}$$

with the jumps per unit length

$$\begin{aligned} \Delta_x^{u_x}/L_x &= 0.1, & \Delta_x^{u_y}/L_x &= -0.2, & \Delta_x^{\phi}/L_x &= 0.5, \\ \Delta_y^{u_x}/L_y &= 0.2, & \Delta_y^{u_y}/L_y &= -0.1, & \Delta_y^{\phi}/L_y &= -0.5. \end{aligned}$$

Note that lemma 1 guarantees that (32) is indeed GP in the x and y directions.

For this synthetic test, we consider the unrealistic material parameters

$$\begin{aligned} E &= 2.5, \quad \nu = 0.25, \\ l &= 1.1, \quad \kappa_L = 1.21, \\ e_L &= 7.2, \quad e_T = 1.33, \quad e_S = 1.73, \\ \mu_L &= 1.5, \quad \mu_T = 1.34, \quad \mu_S = 5.47, \end{aligned}$$

with x as the principal piezoelectric direction. Note that, being a synthetic test, all the involved quantities are unitless and of the same order of magnitude.

Figure 6 shows the evolution of the $\mathcal{L}_2$ error under uniform mesh refinement, for degree $p = 3$ and $p = 4$, with triangular (P) elements of characteristic size $h_k = 0.5^k$ for $k = 2, ..., 5$. The IPM parameter is $\beta_k = 100El^2/h_k$. When no GP is assumed, first Dirichlet boundary conditions (prescribed values of the displacement and the potential) and second Neumann conditions (given value of r) are set on the east, west, south, and north boundaries. When GP is considered only in the x direction, first Dirichlet boundary conditions and second Neumann conditions are set on the south and north boundaries, and $\Delta_x^{u_x}$, $\Delta_x^{u_y}$, Δ_x^{ϕ} are prescribed in the horizontal direction. When GP is considered in both directions, all six jumps are set.

The C0-IPM with GP exhibits the behaviour expected for a C0-IPM formulation for fourth-order PDEs. That is, the convergence rates can be slightly lower that the ones that one would expect in a standard FE method. More precisely, the analysis in [6] for the 2D biharmonic equation, with first and second Dirichlet conditions, concludes that C0-IPM is convergent for degree

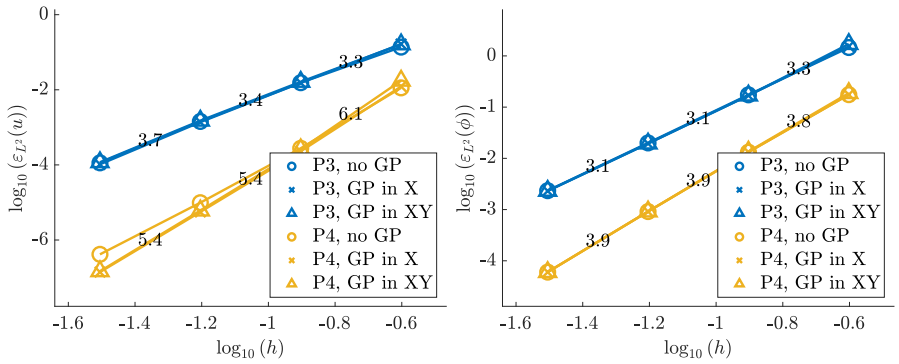

Fig. 6 Convergence plots for the synthetic problem, for the displacement (left) and the potential (right). The numbers are the slope in each segment for the case with GP in the x and y directions.

$p = 2$, but may have convergence rates lower than $p + 1$ depending on the penalty parameter. In the context of flexoelectricity, the numerical tests in [21] show convergence rates around $p + 1$ for the displacement and p for the potential, for degree $p = 3, 4$. Thus, we can conclude that the methodology proposed here, to solve problems with GP, does not compromise the accuracy and convergence of C0-IPM.

6.2 Consistency test 1: GP as a limit behaviour

GP appears in bulk metamaterials as a limit behaviour far away from the boundary. The current example aims at reproducing this behaviour as a validation test. To this end, we consider a unit cell consisting of a solid square of size $L := L_x = L_y = 2.5$ [µm] with a triangular perforation within it with vertexes at $(0.25L, 0.2115L)$, $(0.25L, 0.7885L)$ and $(0.75L, 0.5L)$, and we build a cell array by concatenating it $2N+1$ times along the x direction, as depicted in Figure 7. Note that the choice of an odd number for the cell array length ensures the existence of a central cell.

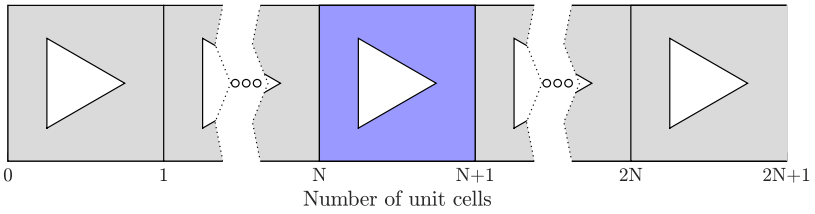

Fig. 7 A cell array made by concatenation of a unit cell with a triangular hole within it. The "zig-zag" gape with three dots indicates that there are many unit cells in between. The numbers in the horizontal axis indicate the number of concatenated unit cells, not the actual x coordinate. The blue shaded unit cell indicates the central cell of the array.

Our goal is to impose boundary conditions that are equivalent to a mechanical compression in the x direction for both the unit cell and the array of cells. For the unit cell we impose GP in the x direction, while for the cell array we will not impose GP, but physical boundary conditions over the whole boundary. What we expect to see is that the solution in the central cell of the array tends to the solution in the unit cell with GP, as we increase the total number of cells $2N+1$.

For this test, we consider triangular elements of degree $p=4$ with characteristic element size $h=0.1L$. The computational mesh for a single unit cell is shown in Figure 8, and the computational meshes for each of the cell arrays is obtained by properly concatenating it $2N+1$ times. Particularly, we test the cell array lengths $(2N+1)=5,11,17,23$.

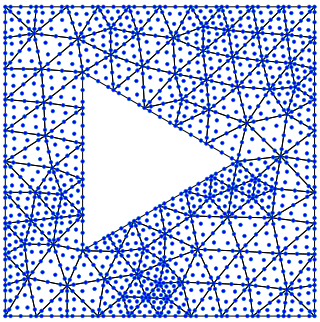

Fig. 8 Computational mesh for the single unit cell, with triangular elements of degree $p=4$ and characteristic size $h=0.1L$.

The material parameters are

$$\begin{aligned} E &= 100\,[\text{GPa}], \quad \nu = 0.37, \\ \kappa &= 11\,[\text{nJ}\,\text{V}^{-2}\,\text{m}^{-1}], \\ e_T &= -4.4\,[\text{J}\,\text{V}^{-1}\,\text{m}^{-2}],\ \mu_T = \mu_L = 1\,[\mu\text{J}\,\text{V}^{-1}\,\text{m}^{-1}], \\ l &= \mu_S = e_S = e_L = 0, \end{aligned} \tag{33}$$

with x taken as the principal piezoelectric direction, and the IPM stabilization parameter is $\beta=1$. The material parameters are realistic, in the sense that they are of the order of magnitude of true flexoelectric materials.

Regarding the boundary conditions, the triangle boundary, and the bottom and top sides of both the unit cell and the cell array, are free boundaries, with homogeneous first and second Neumann conditions. For the unit cell, we impose GP in the x direction and set the increment per unit length values to

$$\Delta_x^{u_x}/L_x = -0.1, \qquad \Delta_x^{u_y} = 0.$$

The jump for the potential per unit length, $\delta_x^\phi = \Delta_x^\phi/L_x$, is free, and it is, in fact, an output of interest. Thus, an homogeneous Neumann macro-condition

is assumed on the potential. For the cell array, at the left and right sides we consider an equivalent compression

$$\boldsymbol{u}(0,y) = (0,0)^T, \quad \boldsymbol{u}((2N+1)L,y) = (\Delta_x^{u_x}(2N+1),0)^T.$$

Note that in the latter we have prescribed the vertical displacements too, which we did not for the unit cell. The idea is that, as N goes to infinity, the central cell of the array should be numb to this difference, and capture the GP phenomena anyways.

Figure 9 (left) shows the evolution of the $\mathcal{L}_2$ difference between the potential distribution, within the centre unit cell of the array, and the single unit cell with GP. The convergence confirms the hypothesis for N going to infinity. Figure 9 (right) shows the evolution of the jump per unit length for the potential at the centre cell of the array, for increasing number of cells. The jump is computed as the difference between nodes that are at the same height, at the left and right sides of the centre cell, for heights $y = 0.1L, 0.5L, 0.6L$. In all cases, the jump per unit length tends to δ_x^ϕ, i.e. to the jump obtained with the single unit cell with GP.

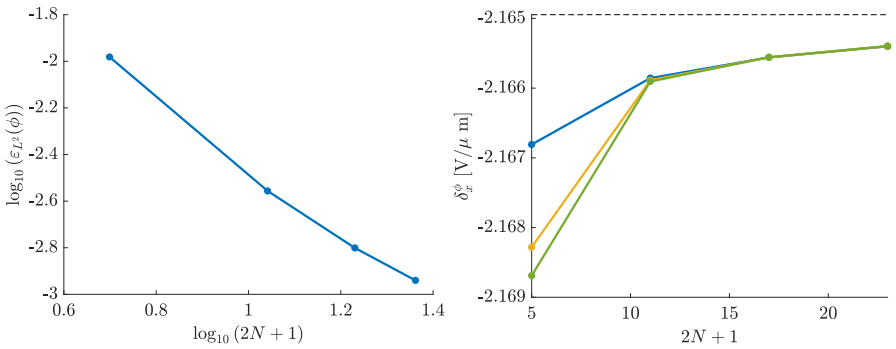

Fig. 9 $\mathcal{L}_2$ difference between the potential distributions of the centre unit cell of the array and the single unit cell with GP, against the number of cells (left), and evolution of the approximation of $\delta_x^\phi = \Delta_x^\phi / L_x$ for the centre unit cell of the array computed as the difference at three different heights. The black dashed line stands for the value of δ_x^ϕ obtained with the single unit cell with GP.

We also observe that the approximation to δ_x^ϕ has 2 correct significant digits with an array of just 5 cells, but the convergence to reduce the difference is slow. A very large computational domain would be needed to capture the limit behaviour of the centre unit cell of the array with higher accuracy. Thus, as expected, solving for a unit cell with GP allows to compute the jump in the potential accurately with far less computational cost.

6.3 Consistency test 2: independence on the choice of the unit cell

The solution to the flexoelectric problem should not depend on the unit cell representative. With this mindset, consider a 2D infinite solid region with circular perforations of radius $r = 0.25L$ and centres $(m, n)L$, where $m, n \in \mathbb{Z}$ and $L = 2.5$ [µm]. This pattern can be obtained by concatenating any of the unit cell representatives depicted in figure 10, among others.

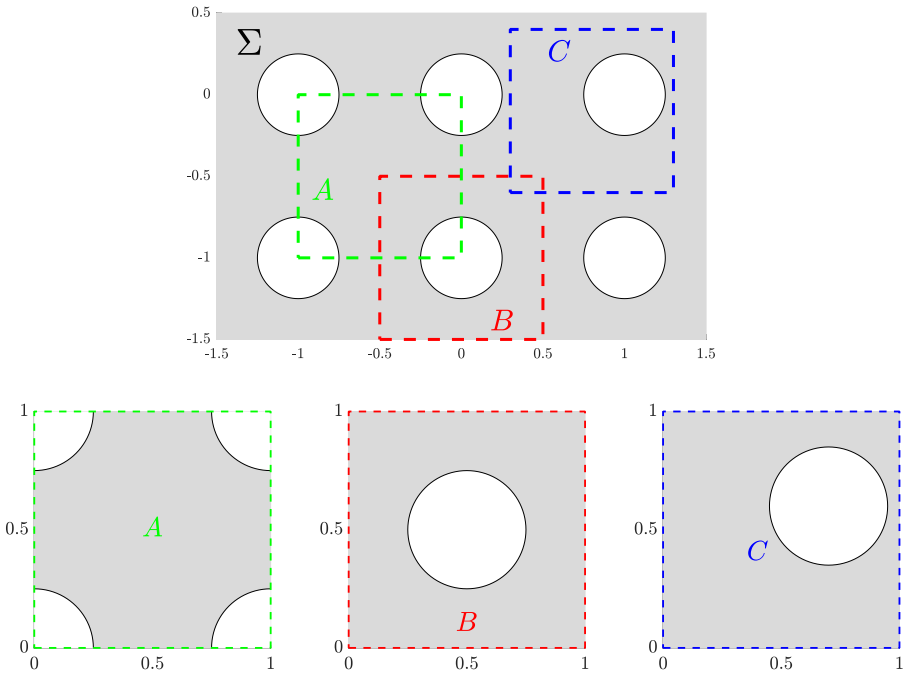

Fig. 10 Portion, Σ, of the 2D infinite pattern, and three different unit cell selections. The x and y axes are adimensionalised (i.e., relative to the cell width $L = 2.5$ [µm]).

A compression is applied in the vertical direction producing a difference (jump) in the potential. That is, we set

$$\Delta_y^{u_x} = 0, \quad \Delta_y^{u_y}/L_y = -0.1,$$

the rest of jumps ($\Delta_x^{u_x}$, $\Delta_x^{u_y}$, Δ_x^{ϕ} and Δ_y^{ϕ}) are let free, and the output of interest is the generated potential difference per unit length, $\delta_y^{\phi} = \Delta_y^{\phi}/L_y$. The material parameters are the ones in equation (33), and y is taken as the piezoelectric direction.

About the computational meshes, triangular elements of degree $p = 4$ are considered, with characteristic sizes $h = 0.1L$ and $h = 0.05L$. The stabilisation parameter is set to $\beta = 1$.

The value of the jump per unit length of the potential δ_y^{ϕ} obtained in each case is shown in table 1. Comparison of the results for each of the element

sizes reveals that the computed values using $h = 0.1L$ already have 4 correct significant digits regardless of the considered unit cell.

δ_y^ϕ [V/µm]	A	B	C	Σ
$h = 0.1L$	-2.23428	-2.23427	-2.23411	-2.23408
$h = 0.05L$	-2.23363	-2.23363	-2.23363	-2.23363

Table 1 Vertical jump of the potential per unit length for the 3 unit cells and the portion domain Σ, for characteristic element size $h = 0.1L$ and $h = 0.05L$.

Figure 11 shows the FEM solutions ϕ_A, ϕ_B, and ϕ_C, for $h = 0.05L$, over each one of the unit cell domains in figure 10; where it is worth recalling that, in this problem, the potential is determined up to a constant. In figure 12 these three solutions are shown together on Σ, setting the constants of the potential to properly patch. The potential obtained solving on Σ with $h = 0.05L$ is also shown for visual comparison. Thus, this test illustrates that the results are indeed independent from the choice of the unit cell representative.

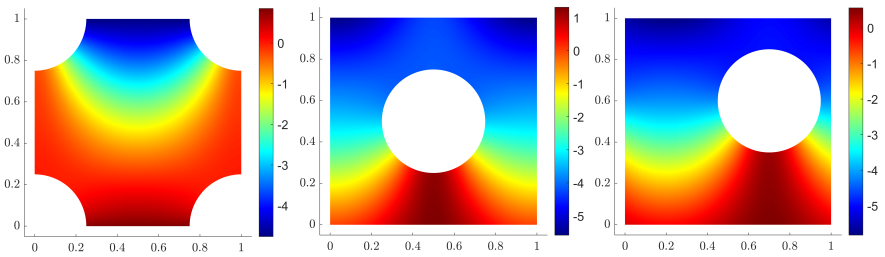

Fig. 11 FEM solution for the electric potential over each one of the considered unit cells, for $h = 0.05L$. The x and y axes are adimensionalised (i.e., relative to the cell width $L = 2.5$ [µm]), and the electric potential is in Volts. The potential is determined up to a constant.

6.4 Some practical examples

A particular application of flexoelectric metamaterials consists on emulating effective piezoelectric response through geometric polarisation of non-piezoelectric materials. In this section, we aim at reproducing some of the results obtained in [17] as a final validation test. We must note, however, that the model considered here is the so-called direct model, whereas the model in [17] considers also converse effects, see [9] for further details. Consequently, their model has two different length scale parameters for the mechanic and electric high-order terms, ℓ_{mech} and ℓ_{elec}, while here we use a single one, l, for the mechanic phenomena only. Accordingly, we set the value of l so that the

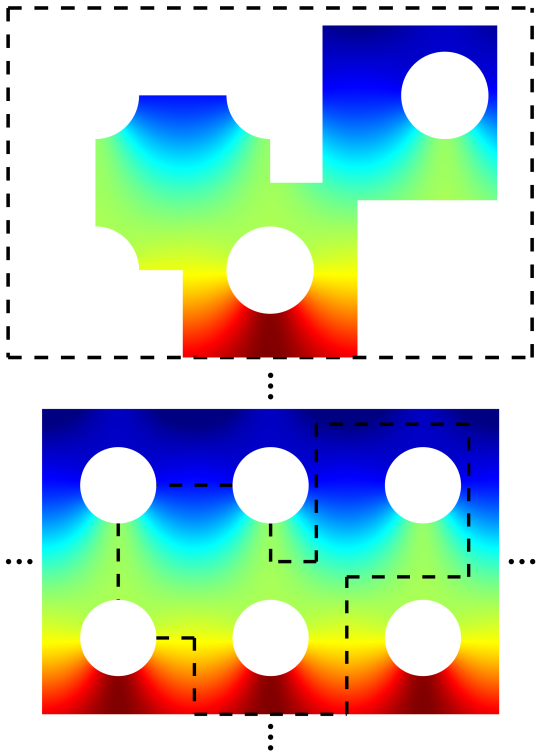

Fig. 12 Electric potential: patched solution from the three different unit cells (top) and solution over Σ (bottom).

ratio l/L_x matches that of ℓ_{mech}/L_x of the model in [17], and we expect to obtain similar results in a qualitative but not quantitative manner.

According to [17], we consider the unit cell geometries shown in Figure 13. The unit cell width is $L_x = L = 5$ [µm] for all unit cells, and the beam width is $0.06L$. The height L_y and the area fraction r_a of each unit cell are shown in table 2. The chosen value for L_x is similar to that used in [17], and the magnitude of the beam width is comparable.

	2d-ch	A	B	C	D
L_y	$1L$	$1L$	$\sqrt{3}L$	$\sqrt{3}L/3$	$\sqrt{3}L/3$
r_a	0.140	0.199	0.177	0.345	0.299

Table 2 Geometric parameters of the unit cell geometries used in the experiment.

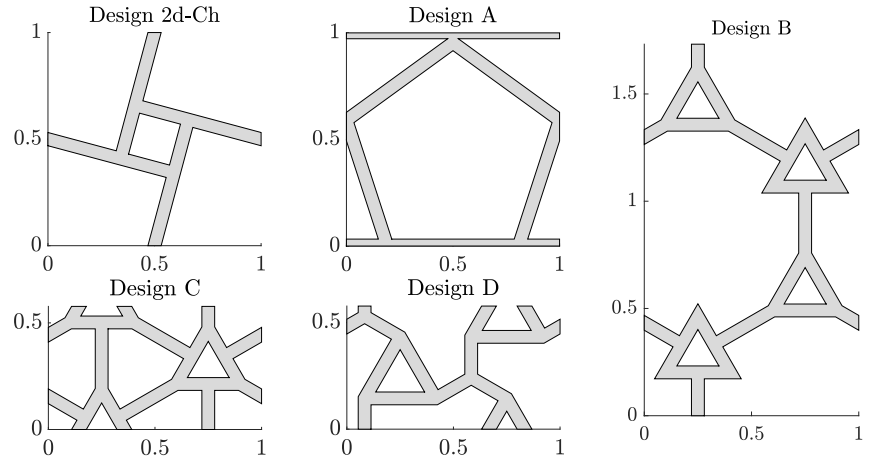

Fig. 13 Sketches of the unit cell geometries used in the experiment, emulating the ones in [17]. The x and y axes are adimensionalised (i.e., relative to the cell width $L = 5$ [µm]).

We take the material parameters used in [17], which correspond to a flexoelectric but non-piezoelectric material,

$$\begin{aligned} &E = 152\,[\text{GPa}], \quad \nu = 0.33, \quad l = 0.01, \quad \kappa = 8\,[\text{nJ}\,\text{V}^{-2}\,\text{m}^{-1}], \\ &\mu_L = 1.21\,[\mu\text{J}\,\text{V}^{-1}\,\text{m}^{-1}], \ \mu_T = 1.10\,[\mu\text{J}\,\text{V}^{-1}\,\text{m}^{-1}], \\ &\mu_S = 0.055\,[\mu\text{J}\,\text{V}^{-1}\,\text{m}^{-1}], \\ &e_T = e_S = e_L = 0, \end{aligned} \tag{34}$$

with y taken as the principal piezoelectric direction.

For the computational meshes, triangular elements of degree $p = 4$ are considered, with characteristic size $h = 0.01L$. The stabilisation parameter is set to $\beta = 100El^2/h$.

Regarding the boundary conditions, a compression is applied in the vertical direction producing a difference (jump) in the potential. Following [17], we set

$$\Delta_y^{u_y}/L_y = -0.1, \quad \Delta_y^{u_x} = \Delta_x^{u_y} = 0,$$

and the rest of the jumps ($\Delta_x^{u_x}$, Δ_x^{ϕ} and Δ_y^{ϕ}) are let free. The output of interest in this experiment is the absolute value of the ratio between the generated potential difference and the input vertical compression, $|\Delta_y^{\phi}/\Delta_y^{u_y}|$, for each one of the unit cell geometries.

The results of the experiment, collected in figure 14, are in qualitative agreement with those in [17], with values of $|\Delta_y^{\phi}/\Delta_y^{u_y}|$ of the same order of magnitude. The only centro-symmetric geometry, namely design 2d-Ch, exhibits a null effective piezoelectric response, as anticipated in [17]. The relative performance of designs A, B, and C, matches that of [17], although the model considered here predicts weaker response for design D. The shown digits are all correct significant digits, and have been checked with finer meshes with characteristic size $h = 0.005L$.

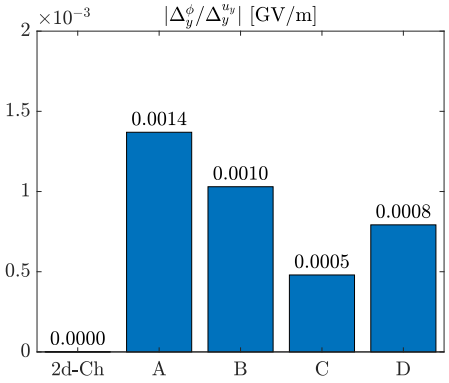

Fig. 14 Absolute value of the ratio between the generated potential difference and the input vertical compression, $|\Delta_y^{\phi}/\Delta_y^{u_y}|$, for each one of the unit cell geometries.

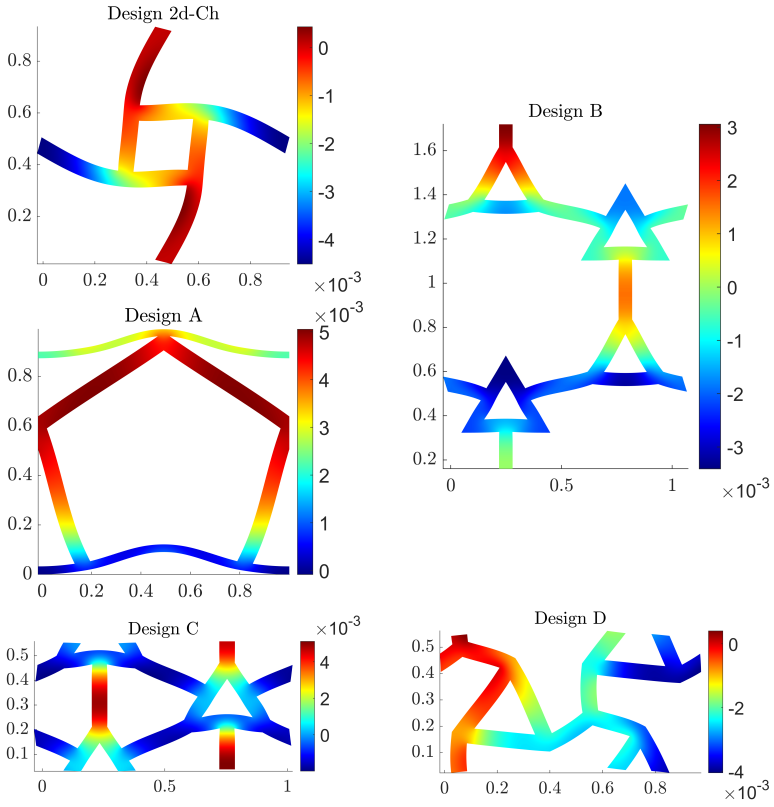

Fig. 15 Electric potential over each one of the deformed unit cell geometries. The x and y axes are adimensionalised (i.e., relative to the cell width $L = 5$ [µm]). The electric potential has been scaled as $\phi/\Delta_y^{u_y}$, and its units are [GV/m].

Figure 15 depicts the FEM solutions for the electric potential over the deformed meshes, for each one of the unit cell geometries, in dimensionless units. The electric potential has been scaled as $\phi/\Delta_y^{u_y}$.

7 Conclusions

The C0-IPM formulation is adapted in this work to solve high-order PDEs with generalised periodicity (GP), with application to the design of flexoelectricity-based metametarials.

The problem is stated in the unit cell with high-order GP conditions, including local and macro conditions. Local GP conditions impose constant jump between opposite sides of the unit cell, as well as $\mathcal{C}^1$ continuity of the displacement and equilibrium of forces, including high-order tractions and corner forces. Macro-conditions can be either Dirichlet, setting a value for the jump, or Neumann, setting the dual quantity. The actual expression of the macro-stresses (electric displacements) is deduced from the weak form derivation as the total sum of the forces (charges) on the unit cell sides.

When the Neumann macro-conditions are assumed to be homogeneous, the resulting C0-IPM weak form is exactly the same as for the standard case, but extending the definition of the jump and the integrals on the interior sides, to include also the sides on the artificial boundary of the unit cell. Taking profit of this, a methodology to introduce GP conditions in an existing standard C0-IPM code, in a straight-forward way, is explained. It is based on identifying opposite sides in the artificial boundary, considering them as interior sides, and using a change of basis matrix to transform the resulting system into the system in the GP space.

All derivations are done in 2D, although they can also be directly applied in 3D, with additional implementation effort. The reduction to strain-gradient elasticity is direct, just considering null material parameters for piezoelectricity and flexoelectricity coupling.

Numerical experiments show that the proposed methodology for problems with GP retains the high-order convergence of the C0-IPM method [21], with convergence of order $p+1$ for the displacement and p for the potential, for approximation degree $p = 3, 4$. The applicability of the formulation in practical situations is also demonstrated, showing consistency with the physical phenomena. Imposing GP conditions on a unit cell successfully captures the limit behaviour of bulk metamaterials, with minimum computational cost. Finally, the results obtained for some specific unit cell geometries of interest are in qualitative agreement with those obtained in previous works.

Acknowledgements This work was supported by the European Research Council (StG-679451 to Irene Arias), Agencia Estatal de Investigación (RTI2018-101662-B-I00), Ministerio de Economía y Competitividad (CEX2018-000797-S) and Generalitat de Catalunya (2017-SGR-1278)

Data availability statement

Data sharing is not applicable to this article as no datasets were generated or analysed during the current study. The information to reproduce the numerical results is included in the paper.

Declarations

Beyond the received support stated in the acknowledgements, the authors have no further competing interests to declare that are relevant to the content of this article.

References

1. Abdollahi, A., Peco, C., Millán, D., Arroyo, M., Arias, I.: Computational evaluation of the flexoelectric effect in dielectric solids. Journal of Applied Physics **116**, 093502–093502 (2014)
2. Balcells, O.: Computational modelling of flexoelectricity-based 2D metamaterials. Master's thesis, Universitat Politècnica de Catalunya (2021). URL https://upcommons.upc.edu/handle/2117/349212
3. Barceló-Mercader, J., Codony, D., Marco, O., Fernández-Méndez, S., Arias, I.: Weak enforcement of interface continuity and generalized periodicity in high-order electromechanical problems. International Journal for Numerical Methods in Engineering **123**, 901–923 (2022)
4. Brenner, S.C., Gu, S., Gudi, T., Sung, L.Y.: A quadratic C0 interior penalty method for linear fourth order boundary value problems with boundary conditions of the Cahn-Hilliard type. SIAM Journal on Numerical Analysis **50**(4), 2088–2110 (2012)
5. Brenner, S.C., Gu, S., Gudi, T., Sung, L.y.: A quadratic c0 interior penalty method for linear fourth order boundary value problems with boundary conditions of the cahn–hilliard type. SIAM Journal on Numerical Analysis **50**(4), 2088–2110 (2012)
6. Brenner, S.C., Sung, L.Y.: C0 Interior Penalty Methods for fourth order elliptic boundary value problems on polygonal domains. Journal of Scientific Computing **22**(1), 83–118 (2005)
7. Codony, D., Gupta, P., Marco, O., Arias, I.: Modeling flexoelectricity in soft dielectrics at finite deformation. Journal of the Mechanics and Physics of Solids **146**, 104182 (2021)
8. Codony, D., Marco, O., Fernández-Méndez, S., Arias, I.: An immersed boundary hierarchical B-spline method for flexoelectricity. Computer Methods in Applied Mechanics and Engineering **354**, 750 – 782 (2019)
9. Codony, D., Mocci, A., Barceló-Mercader, J., Arias, I.: Mathematical and computational modeling of flexoelectricity. Journal of Applied Physics **130**, 231102 (2021)
10. Deng, F., Deng, Q., Yu, W., Shen, S.: Mixed Finite Elements for Flexoelectric Solids. Journal of Applied Mechanics **84**(8) (2017)
11. Engel, G., Garikipati, K., Hughes, T., Larson, M., Mazzei, L., Taylor, R.: Continuous/discontinuous finite element approximations of fourth-order elliptic problems in structural and continuum mechanics with applications to thin beams and plates. Computer Methods in Applied Mechanics and Engineering **191**, 3669–3750 (2002)
12. Fojo, D., Codony, D., Fernández-Méndez, S.: A C0 Interior Penalty Method for 4th order PDEs. Reports@SCM (2020). URL (early view) http://revistes.iec.cat/index.php/reports/article/view/148126/145828
13. Ghasemi, H., Park, H.S., Rabczuk, T.: A level-set based IGA formulation for topology optimization of flexoelectric materials. Computer Methods in Applied Mechanics and Engineering **313**, 239 – 258 (2017)
14. Kshetrimayum, R.: A brief intro to metamaterials. IEEE Potentials **23**(5), 44–46 (2005)

15. López, J., Valizadeh, N., Rabczuk, T.: An isogeometric phase-field based shape and topology optimization for flexoelectric structures. Computer Methods in Applied Mechanics and Engineering **391**, 114564 (2022)
16. Mao, S., Purohit, P., Aravas, N.: Mixed finite-element formulations in piezoelectricity and flexoelectricity. Proceedings of the Royal Society A: Mathematical, Physical and Engineering Science **472**, 20150879 (2016)
17. Mocci, A., Barceló-Mercader, J., Codony, D., Arias, I.: Geometrically polarized architected dielectrics with apparent piezoelectricity. Journal of the Mechanics and Physics of Solids **157**, 104643 (2021)
18. Nanthakumar, S., Zhuang, X., Park, H.S., Rabczuk, T.: Topology optimization of flexoelectric structures. Journal of the Mechanics and Physics of Solids **105**, 217 – 234 (2017)
19. Qing-Sheng Yang, W.B.: A comparative investigation of different homogenization methods for prediction of the macroscopic properties of composites. Computer Modeling in Engineering & Sciences **6**(4), 319–332 (2004)
20. Shu, L., Liang, R., Rao, Z., Fei, L., Ke, S., Wang, Y.: Flexoelectric materials and their related applications: A focused review. Journal of Advanced Ceramics **8**(2), 153–173 (2019)
21. Ventura, J., Codony, D., Fernández-Méndez, S.: A C0 interior penalty finite element method for flexoelectricity. Journal of Scientific Computing **88**(3), 88 (2021)
22. Zhuang, X., Nguyen, B., Nanthakumar, S., Tran, T., Alajlan, N., Rabczuk, T.: Computational modeling of flexoelectricity. A review. Energies **13**, 1326 (2020)
23. Zouhdi, S., Sihvola, A., Vinogradov, A.: Metamaterials and Plasmonics: Fundamentals, Modeling, Applications. Springer (2008)